

**MODELING AND SIMULATION OF SOLID PARTICLE EROSION  
OF PROTECTIVE FILMS**

A Thesis

by

**SOURAV BANERJEE**

Submitted to the Office of Graduate Studies of  
Texas A&M University  
in partial fulfillment of the requirements for the degree of

**MASTER OF SCIENCE**

December 2010

Major Subject: Aerospace Engineering

**MODELING AND SIMULATION OF SOLID PARTICLE EROSION  
OF PROTECTIVE FILMS**

A Thesis

by

SOURAV BANERJEE

Submitted to the Office of Graduate Studies of  
Texas A&M University  
in partial fulfillment of the requirements for the degree of

MASTER OF SCIENCE

Approved by:

Co-Chairs of Committee,	Amine Benzerga
	Ramesh Talreja
Committee Member,	Anastasia Muliana
Head of Department,	Dimitris Lagoudas

December 2010

Major Subject: Aerospace Engineering

## ABSTRACT

Modeling and Simulation of Solid Particle Erosion  
of Protective Films. (December 2010)

Sourav Banerjee, B.E., Anna University, India

Co-Chairs of Advisory Committee: Dr. Amine Benzerga  
Dr. Ramesh Talreja

Among many useful properties of elastomers, one is their ability to absorb energy by deforming to large strains without fracturing. This property combined with their good adhesion to substrates makes them suited as adhesive films and coatings for protection against impact damage. An example of practical significance is the erosion of helicopter rotor blades where the protection of leading edge is often achieved by mounting a film or applying a coat of polyurethane. Although this is a workable solution, there is currently little knowledge as to the durability of this elastomeric film/coat under impact of hard and angular particles such as sand. A deformation and failure analysis that deals with the angularity of the erodents and captures the local mechanisms responsible for erosion damage in elastomers is the *sine qua non*. The present endeavor tries to address these issues by considering a polyurethane layer on a quasi-rigid substrate, impacted by hard particles at velocities and angles of attack given by pre-specified distributions. A novel method is devised to address the angularity issue. A series of finite-element calculations

are performed on the coating layer-substrate systems subjected to different velocities, incidence and angularity of the impacting erodents. An elasto-plastic material constitution with isotropic hardening is employed in the simulations and material parameters representative of polyurethane are used for the coat. Initial parametric deformation analyses provided an adequate qualitative estimate of erosion parameters. Incorporation of a stress based fracture criterion enabled a quantitative measure of material removal due to erosion to be achieved. The simulation results show good match with experimental trends of target mass loss as obtained under normal and inclined loadings with angular erodents. The current simulation framework has sufficient capability and versatility to incorporate more enriched polymer-models and advanced fracture criteria in the future, thereby allowing parametric studies toward selection of materials and coat-layer thicknesses thus predicting the erosion mass loss as accurately as measured by experiments.

## **DEDICATION**

To my parents, and to Dr. (Sqn. Ldr.) B.S.M Augustine and Dr. Satish Chandra

## **ACKNOWLEDGEMENTS**

I would like to express my sincere thanks to my advisor, Dr. Amine Benzerga, for the timely guidance, astute philosophy and rigor he imparted on me during the duration of this research. I would also like to express my deepest gratitude to my co-advisor, Dr. Ramesh Talreja, for the inimitable support, academic insights and stimulating conversations that he provided during the entire endeavor. Every moment spent with my advisors was enlightening beyond imaginations.

I am also indebted to my research committee member, Dr. Anastasia Muliana, for her time and effort in evaluating this research.

Thanks also go to my friends and colleagues and the department faculty and staff for making my time at Texas A&M University a great experience.

## NOMENCLATURE

NR	Natural Rubber
PUR	Polyurethane
PBC	Periodic Boundary Condition
SEM	Scanning Electron Micrograph

## TABLE OF CONTENTS

	Page
ABSTRACT .....	iii
DEDICATION.....	v
ACKNOWLEDGEMENTS .....	vi
NOMENCLATURE .....	vii
TABLE OF CONTENTS .....	viii
LIST OF FIGURES .....	x
LIST OF TABLES.....	xii
 1. INTRODUCTION .....	 1
1.1. Motivation.....	1
1.2. Organization of Sections.....	3
 2. LITERATURE SURVEY .....	 4
2.1. Experimental Findings on Erosion .....	4
2.2. Analytical Models of Erosion .....	10
2.3. Computational Approaches to Erosion.....	15
2.3.1. Erosion Simulation .....	15
2.3.2. Material Models Used in Simulation .....	18
2.4. Lessons from Literature Survey .....	20
 3. PROBLEM FORMULATION .....	 23
3.1. Research Objective .....	23
3.2. Simulation Framework .....	23
3.2.1. Type of Analyses .....	23
3.2.2. Model Geometry and Mesh.....	25
3.2.3. Boundary Conditions .....	28
3.2.4. Material Models.....	30



3.2.5. Fracture Model .....	32
4. MATERIAL PARAMETER IDENTIFICATION.....	33
4.1. Deformation .....	33
4.2. Fracture .....	35
5. RESULTS AND DISCUSSION.....	37
5.1. Deformation Analysis.....	37
5.2. Failure Analysis.....	44
5.2.1. Impact with Spherical Erodents.....	44
5.2.2. Impact with Sharp Erodent.....	57
6. SUMMARY AND CONCLUSION .....	62
REFERENCES .....	64
APPENDIX A .....	68
VITA .....	81

## LIST OF FIGURES

	Page
Figure 2-1 Brittle erosion crater (a) side view, (b) top view.....	4
Figure 2-2 Ductile erosion crater (a) side view, (b) top view .....	5
Figure 2-3 Ductile erosion: (a) primary and secondary damage, (b) trapped erodent. ...	5
Figure 2-4 SEM of section of NR eroded at 90 deg by 120 mesh sand at 70m/s, showing fine subsurface cracks .....	6
Figure 2-5 SEM of top surface of NR eroded at 90 deg by 120 mesh sand at (a) 90m/s, and (b) 140 m/s showing formation of erosion pits .....	7
Figure 2-6 Transverse ridges in NR eroded by 120 mesh sand at 30 degrees and 100 m/s (a) top view, (b) side view .....	8
Figure 2-7 Transverse ridges in NR at 30 m/s.....	8
Figure 2-8 Transverse ridges in NR at 140 m/s.....	8
Figure 2-9 Effect of angularity on erosion rate of chalk. ....	9
Figure 2-10 Erosion of aluminum at (a) 10m/s, (b) 107 m/s.....	12
Figure 2-11 Variation of erosion rate in rubbers with increasing velocity under normal impact by sand .....	13
Figure 2-12 Predicted erosion rate for rubbers .....	14
Figure 2-13 Measured erosion rate for rubbers .....	14
Figure 2-14 FEM model and eroded surface.....	16
Figure 2-15 Weight loss vs. erodent mass flow .....	16
Figure 2-16 Erosion rate vs. incidence angle for ElTobgy FE model and other analytical models .....	16
Figure 2-17 Deformed surface after non-coincident and stochastic impact 10, 100 and 200 particles.....	17
Figure 3-1 Target material impinged by erodent particles .....	24
Figure 3-2 Target geometry showing finite element mesh with characteristic dimensions .....	26
Figure 3-3 Finite element mesh of spherical erodent showing characteristic length....	27

	Page
Figure 3-4 Finite element mesh and characteristic length of ‘sharp erodent’ .....	27
Figure 3-5 Annulus method for describing angularity .....	29
Figure 3-6 Periodicity and angularity description .....	29
Figure 4-1 Stress - strain response of PUR thin film under uniaxial tension .....	34
Figure 4-2 Elasto-plastic approximation of PUR macroscopic behavior .....	34
Figure 4-3 PUR tensile test till fracture .....	36
Figure 5-1 Iso-surfaces of contours of plastic strain after 5 vertical impacts at 50m/s. 41	41
Figure 5-2 Time history of plastic strain for different angularities and multiple impacts .....	42
Figure 5-3 Side view of deformed target after 5 coincident hits. ....	42
Figure 5-4 Effect of angularity on volume of impact crater .....	43
Figure 5-5 Impact at 50 m/s with d/s 0.3 and critical stress 12.5 MPa. ....	47
Figure 5-6 Impact at 125 m/s with d/s 0.3 and critical stress 12.5 MPa. ....	48
Figure 5-7 Topography of eroded PUR target after impact at 125 m/s by d/s 0.3 spherical erodent.....	52
Figure 5-8 Erodent capture at perpendicular impact (a) simulation, (b) experiments..	52
Figure 5-9 Mass loss vs. impact velocity for perpendicular impact and d/s 0.1. ....	53
Figure 5-10 Mass loss vs. impact velocity after 2 perpendicular impacts. ....	53
Figure 5-11 Mass loss vs. angularity after 2 perpendicular impacts. ....	54
Figure 5-12 Mass loss vs. angularity at 100 m/s impact velocity.....	54
Figure 5-13 Histograms of erosion mass loss for different critical stresses.....	55
Figure 5-14 Mass loss vs. impact angle. ....	56
Figure 5-15 Inclined impact by a spherical erodent, d/s 0.1, 150 m/s. ....	56
Figure 5-16 Topography of eroded mesh after impact by sharp erodent. ....	58
Figure 5-17 Isosurfaces of contours of effective stress in the PUR target. ....	59
Figure 5-18 Isosurfaces of contours of plastic strain on deformed zone. ....	60
Figure 5-19 Mass loss vs. impact angle erosion curve for sharp erodent. ....	61

**LIST OF TABLES**

	Page
Table 2-1 Erosion variables.....	20
Table 4-1 Material parameters used in simulation.....	35

## 1. INTRODUCTION

### 1.1. MOTIVATION

In the past, studies of solid particle erosion were of substantial interest in connection with a variety of industrial problems. Erosive environments can be extremely detrimental to the service-life and performance of components made out of metals and alloys including the blades and disks of aircraft compressors, helicopter rotor blades, and valves, piping and centrifugal pumps used in industrial waste water systems, municipal sewage plants, sea-water systems and for the transport of slurry in pulp and paper industry. Among other erosion problems which occur in industry are those connected with the equipment used in the catalytic cracking of oil or coal turbines, hydraulic turbines, and coal hydrogenation. While usually considered undesirable, erosion can sometimes be beneficial and have useful application in such processes as sand blasting, abrasive deburring and the erosive drilling of hard materials. It is also used for decoration of window glass and mirrors, where the damage generates an optical effect on the glass surface. In a new development, the latter method is extended for generating technical patterns such as holes and canals in brittle substrates. In this area, well controllable solid particle erosion is a desired phenomenon. Two-body abrasion, three-body abrasion, powder-blasting etc. are important finishing and material removing processes in a wide range of industrial operations.

Much investigation has been devoted to identifying the variables that influence erosion so that adequate prevention schemes can be adopted or, in the useful cases, in order to harness the full potential of erosion. However, even after four decades, no

---

This thesis follows the style of Computer Methods in Applied Mechanics and Engineering.

homogenization of the different types of erosion parameters was possible. The effort was further complicated with the introduction of polymers and composites. Because of their very high specific stiffness and strength, polymers and their composites are now used extensively in a multitude of applications. Other than the industrial applications already mentioned one can add aircraft canopies, radomes, automotive-wind screens, rocket-nozzles and outer space applications; fibrous ceramic components e.g. alumino-silicates are widely used as lining materials in high temperature applications such as power plant and industrial furnaces. In all these applications, the components are subjected to degradation by abrasive gas-jets or rain or erosion by dust and other solid particles. Often, polymeric coatings are used to protect composite structures from rain and solid particle erosion; it was found by trial that resilient elastomeric coatings can provide optimum protection with minimal erosion.

Polyurethane elastomers are being used as wear-resistant materials to replace traditional metallic or ceramic materials in the mineral and mechanical industries and are expanding in aerospace and other corresponding fields. However, the drawbacks for Polyurethane elastomers, as wear-resistant materials, such as poor heat resistances, high costs etc have provided a new perspective to the field of erosion studies. The thrust now would be to develop analytical or simulation models that would adequately address the issues of erosive wear of such materials and their coatings. If any further notable progress is to be made in the field, such an endeavor would require incorporation, from the very inception, of appropriate material deformation and fracture models along with the other erosion parameters and also the inclusion of previously unaddressed variables like erodent angularity or sharpness.

## 1.2. ORGANIZATION OF SECTIONS

This study on erosion simulation of polyurethane films impacted by sand particles has been organized into six sections. Section 1 introduces the motivation behind the entire endeavor by discussing the influences of solid particle erosion in industrial and military applications.

Section 2 covers the literature review of the problem by introducing the salient experimental facts as observed over the years in sand blasting experiments. Analytical models which try to predict the observed experimental trends are also discussed, followed by computational methods employed so far to study erosion; finally the lessons learnt from the literature survey are stated thereby paving a roadmap to define a simulation methodology for the current study.

Section 3 defines the objective of this endeavor and the goals to be accomplished and also introduces the simulation framework, viz. model geometries, material deformation and fracture models etc., to be employed in all subsequent computational analyses. Determination of material deformation and fracture parameters which enter the simulation framework is dealt with in Section 4.

Section 5 analyzes the results obtained from the series of finite-element calculations performed according to the test cases defined in the previous section. Furthermore, it discusses few of the roadblocks encountered during erosion simulation and also attempts to correlate these to the obtained results, experimental trends and the anticipated mechanisms of erosion.

Section 6 summarizes important findings, concludes this research and discusses the future follow-up work to be carried out.

## 2. LITERATURE SURVEY

### 2.1. EXPERIMENTAL FINDINGS ON EROSION

A wealth of practical information is available on erosive wear, which indicates that erosion due to solid particle impact can be subdivided into two parts based on the incident angle of the flow in which the erodent is entrenched; these are normal and oblique impacts and the corresponding erosion mechanisms being called ‘Deformation wear’ and ‘Cutting Wear’ respectively [1-3]. The state-of the art in erosion experimentation has been sand-blasting techniques or vacuum free-fall apparatus, in both of which, a semblance of control can be achieved with respect to the flow velocity, incident angle and erodent size. Such experimentation revealed that at normal or near normal incidence, repeated impact by the erodent causes deformation hardening which tends to make the exposed surface more brittle; subsequent impacts leads to the formation of lateral and radial cracks resulting in chipping or spallation of the material, this is also called brittle-erosion (Figure 2-1).

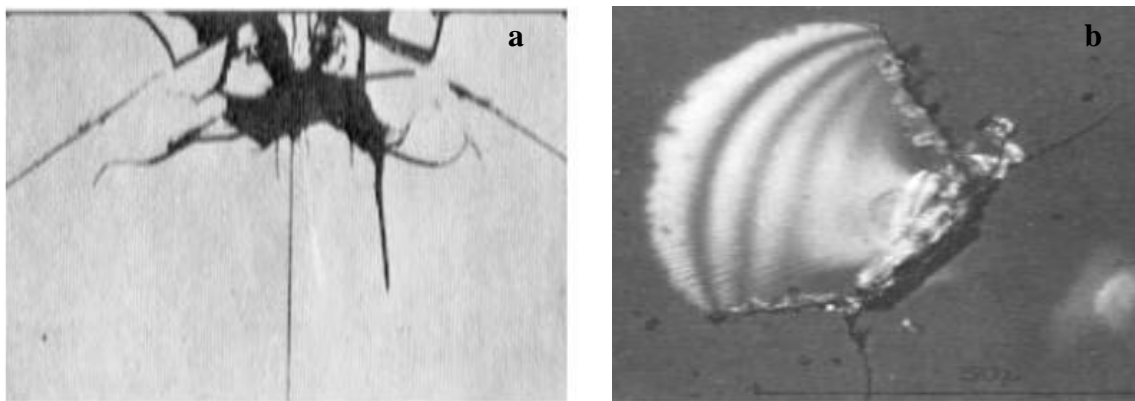


Figure 2-1 Brittle erosion crater (a) side view, (b) top view. Adapted from [3, 4] respectively

At oblique angles wear phenomenon is also called ductile erosion because it is predominant in ductile materials; the material removal involves removal of chips from



the surface in a cutting type of action. Close inspection of the scratches at different angles revealed that the material is extruded in the direction of impact and towards the sides to form relatively fragile lips or protrusions (Figure 2-2) which are very vulnerable to subsequent impacts.

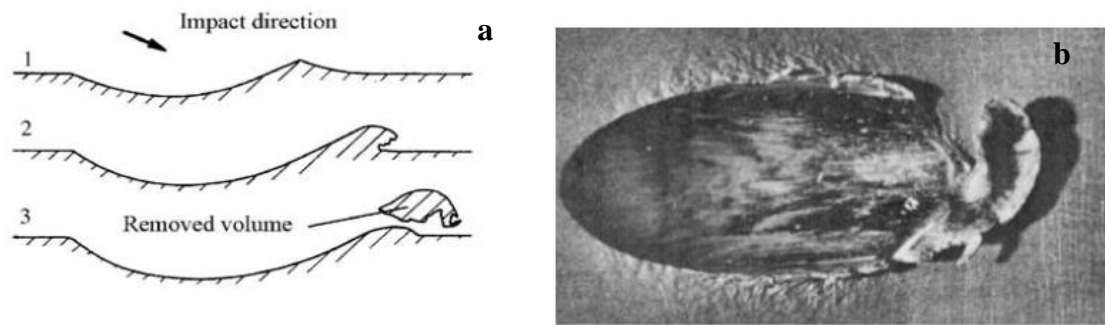


Figure 2-2 Ductile erosion crater (a) side view, (b) top view Adapted from [4]

In addition, high speed photography has shown that erodent particles disintegrate on impact so that small fragments are thrown away from the primary scars to produce secondary damage. Sometimes the erodent burrows inside the target material and gets trapped (causing an initial increase of mass of the target) only to be freed later by impacts of subsequent particles or loss of the adjacent material. These are evident in Figure 2-3.

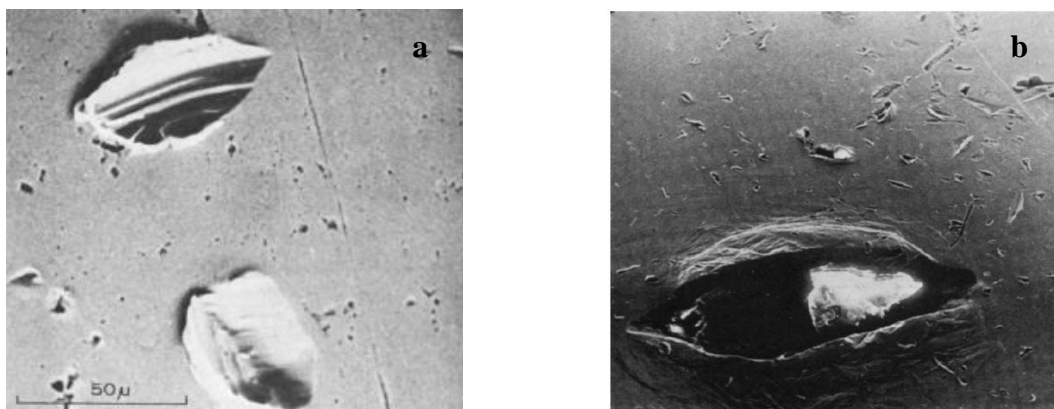


Figure 2-3 Ductile erosion: (a) primary and secondary damage, (b) trapped erodent.  
Adapted from [5] and [3] respectively

In the case of hard and brittle materials cutting wear is negligibly small in relation to deformation wear, whereas for soft and ductile materials the reverse may be true. According to Bitter [1, 6] the two types of erosion occurs simultaneously and the total erosion is a summation of deformation and cutting wear.

The erosion process of elastomers, which is of primary interest in this endeavor, also exhibits two separate mechanisms [7]; one dominating at glancing angles of impact, the other taking over under conditions of normal impact. In both mechanisms, material is removed from the surface by fatigue crack propagation. At high impact angles, tensile stresses in the surface arising from the frictional forces due to particle impact causes fine cracks to grow progressively into the surface (Figure 2-4), target material loss occurs wherever these cracks intersect and chips away the surface.

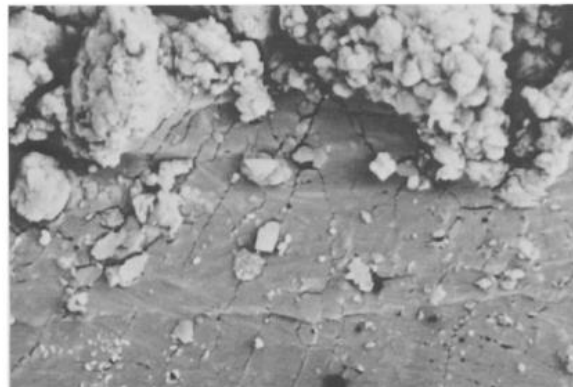


Figure 2-4 SEM of section of NR eroded at 90 deg by 120 mesh sand at 70m/s, showing fine subsurface cracks [7]

At normal incidence and velocities lower than 120 m/s, only a network of cracks are found on a relatively smooth surface; whereas at velocities of 140 m/s and higher, erosion rate rapidly increases, probably due to the formation of wide and deep pits around which the surface is very rough and almost granular. Figure 2-5 shows these features from an

eroded sample of natural rubber (NR) subjected to sand-flow velocities of 90m/s and 140m/s at 90 degrees incidence.

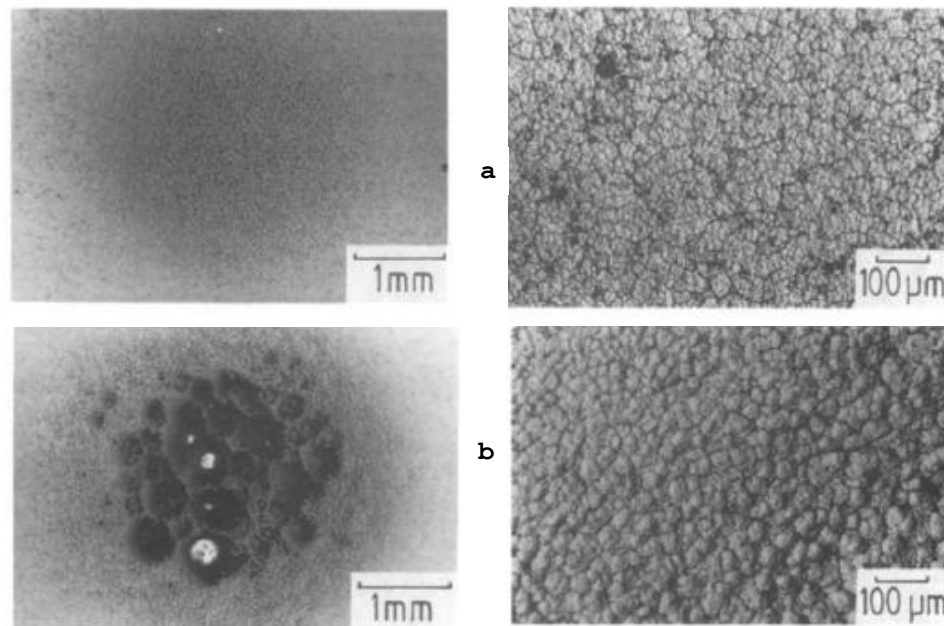


Figure 2-5 SEM of top surface of NR eroded at 90 deg by 120 mesh sand at (a) 90m/s, and (b) 140 m/s showing formation of erosion pits [7]

In the case of glancing impact on rubbers or elastomers, the mechanism of material removal has been found to be very similar to that occurring during sliding abrasion by a blade or by a smooth indenter. Figure 2-6 illustrates this phenomenon, where a series of ridges, running transversely to the impact direction, is produced during the initial stages of erosion. The specimen of NR in this case was eroded by 120 mesh sand at 30 degrees and 100 m/s; flow direction was from the left for Figure 2-6 (a) and from the right for Figure 2-6 (b).

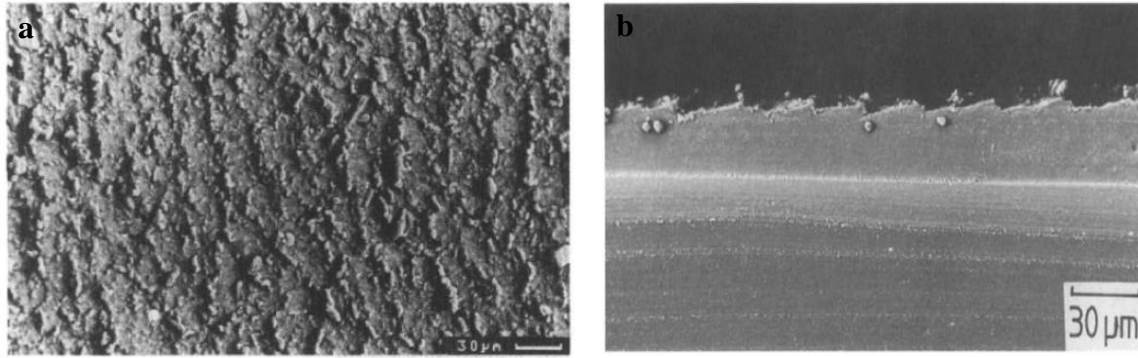


Figure 2-6 Transverse ridges in NR eroded by 120 mesh sand at 30 degrees and 100 m/s  
(a) top view, (b) side view. Adapted from [8] and [7] respectively

Figure 2-6 (b) is an SEM micrograph of a transverse section through the eroded area. There is very little subsurface damage and it can be seen that the ridges are generally sawtoothed in shape, with the steeper face towards the direction of erosion.

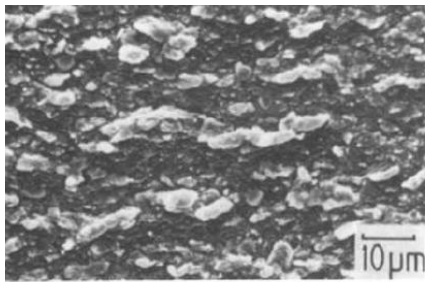


Figure 2-7 Transverse ridges in NR at 30 m/s [7]

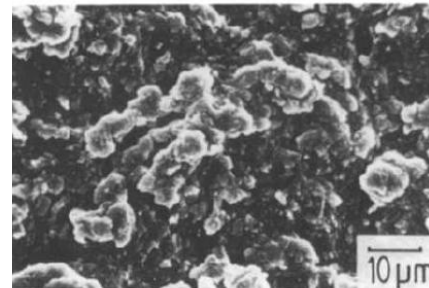


Figure 2-8 Transverse ridges in NR at 140 m/s [7]

Figure 2-7 and Figure 2-8 show that a higher erosion rate leads to less-well-defined ridges. Visibly, the features produced at the low velocity are very well-defined transverse ridges; however the ridges are much more broken up and less well aligned at the higher impact velocity. These features show a remarkable similarity to those seen on abraded elastomer surfaces. Impacting particles slide over the surface and deform the ridges, causing the growth of fatigue cracks from the base of each ridge. These characteristics have also been taken advantage in formulating a model for erosion of rubber at oblique impacts [8].

It has often been reported in literature [9-12] that sharp or angular erodents tend to lead to higher rates of erosion. Though the trend seems to be trivial, the exact reason behind the phenomena has not yet been identified, plagued by the lack of understanding of the underlying mechanisms of erosion and by the complexities in characterizing arbitrary shapes of angular erodents. Slikkerveer et al. [11] and Stachowiak [12] had undertaken the task of characterizing particle shapes and provided various statistical techniques for describing particle angularity. Whereas many of these statistical parameters perform well as descriptors of sharpness, their inherent complexity hinders their incorporation into existing analytical or simulation models for addressing erosion due to sharp particles.

Nonetheless, these efforts put emphasis on the fact that so far not much focus has been given on erodent angularity though it plays a predominantly detrimental role to the eroded surface as shown in Figure 2-9 where the erosion rates in chalk has been plotted for different types of erodents with varying angularity.

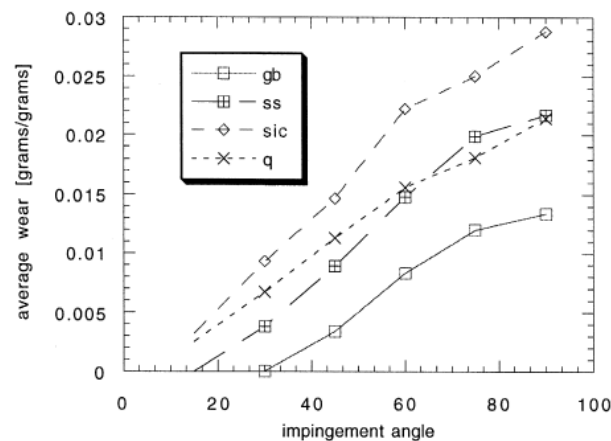


Figure 2-9 Effect of angularity on erosion rate of chalk.

Expansion of legend: Glass bead, Silica Sand, Silicon Carbide, Quartz; Adapted from [12]

## 2.2. ANALYTICAL MODELS OF EROSION

The analytical approaches are directed towards developing equations relating the erosion parameters and variables in order to predict the effect of erosion on component life and functionality. So, it is of considerable relevance to attempt to identify if any such existing ‘Erosion-Model’ can be applied, directly or with rational manipulation of the variables, to the sand-erosion of polyurethane elastomers.

A detailed literature survey revealed that more than 30 such models exist solely for addressing solid particle erosion. Most have their own reasoning and rationale and can be classified either as empirical, contact-mechanics based or, less frequently, material-failure mechanism based. Meng and Ludema [13] have provided a detailed list of these erosion-wear models and also suggested guidelines for the future development of such models.

Among the multitude of models, one model which has found mention in majority of credible publications is that of Bitter [1, 6]. Bitter’s model is based on Hertzian Contact mechanics. Using an energy based approach it predicts the volume lost due to erosion in both normal and oblique impact cases. This model is intricate as it accounts for elasto-plastic deformation of both the target and the erodent. However, other than the inherent limiting assumptions of Hertzian contact, few other drawbacks of this model are that it does not account for the repeated cyclic event of impact which characterizes any erosion process and furthermore, it requires erosion experiments on the material of interest to assess the values of few unknown parameters required to calibrate the model.

The following relations sum-up Bitter’s Model for Solid Particle Erosion

$$W_{\text{total}} = W_d + W_c$$

$W_d$  –erosion due to deformation wear (in volume units)

$W_c$  –erosion due to cutting wear (in volume units)

$$W_d = \begin{cases} \frac{M[V \sin \alpha - V_{el}]^2}{2\varepsilon_b}, & V \sin(\alpha) > V_{el} \\ 0, & V \sin(\alpha) < V_{el} \end{cases} \quad (1)$$

$$W_c = \begin{cases} \frac{2MC'[V \sin \alpha - V_{el}]^2}{\sqrt{V \sin \alpha}} \times \left[ V \cos \alpha - \frac{C'[V \sin \alpha - V_{el}]^2}{\sqrt{V \sin \alpha}} \phi_c \right], & \alpha \leq \alpha_0 \\ \frac{M\{V^2 \cos^2 \alpha - K_1[V \sin \alpha - V_{el}]^{3/2}\}}{2\phi_c}, & \alpha \geq \alpha_0 \end{cases} \quad (2)$$

where

$$V_{el} = \frac{1.54\sigma_y^{5/2}}{\sqrt{\rho_p}} \left[ \frac{1 - \nu_p^2}{E_p} + \frac{1 - \nu_t^2}{E_t} \right] \quad (3)$$

$$K_1 = 0.82\sigma_y^2 \sqrt{\frac{\sigma_y}{\rho_t}} \cdot \left[ \frac{1 - \nu_p^2}{E_p} + \frac{1 - \nu_t^2}{E_t} \right] \quad (4)$$

$$C = \frac{0.288}{\sigma_y} \sqrt[4]{\frac{\rho_t}{\sigma_y}} \quad (5)$$

$M$  and  $V$  - total mass and velocity of impinging particles

$\alpha$  - impact angle

$\alpha_0$  - impact angle at which the horizontal velocity component has just become zero when the particle leaves the body

$V_{el}$  and  $K_1$ - Threshold Velocities for Deformation and Cutting Wear respectively.

$\varepsilon_b$  and  $\phi_c$  - energy needed to remove a unit volume of material from the body surface under deformation wear and cutting wear respectively; describes the elasto-plastic behavior of the substance; derived from erosion experiments.

Subscripts 'p' and 't' stands for particle and target respectively.

The drawbacks notwithstanding, predictions from this model show good agreement to data from erosion experiments of metals at different velocities and angles of impingements as shown in Figure 2-10.

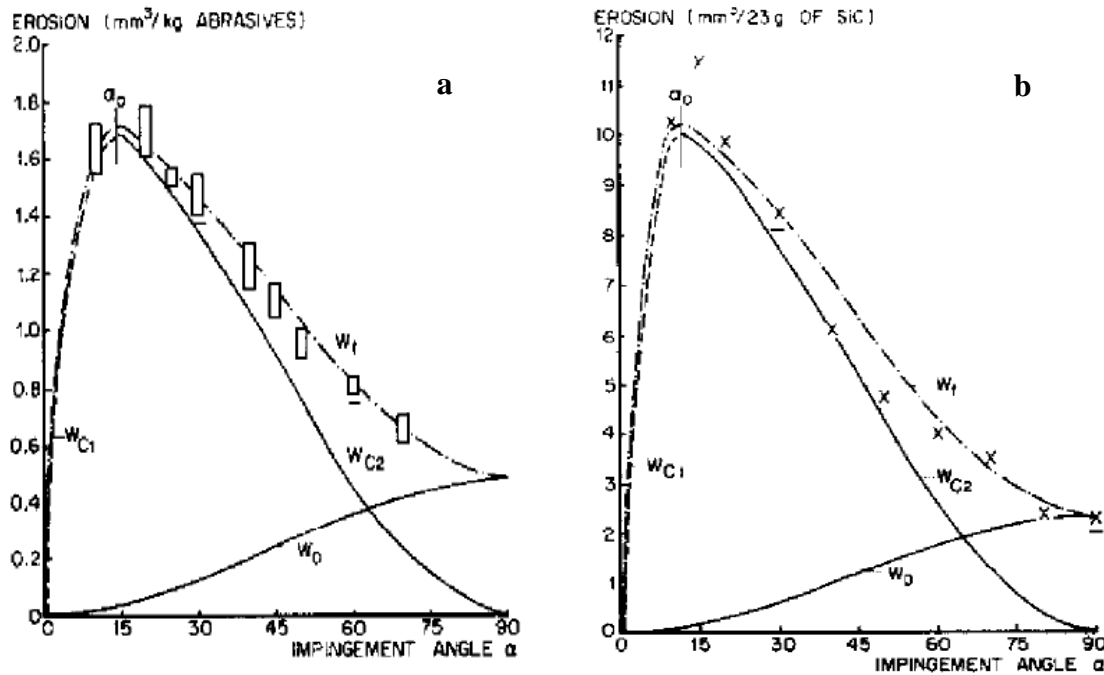


Figure 2-10 Erosion of aluminum at (a) 10m/s, (b) 107 m/s. Adapted from [6]

One of the most prominent names in the field of erosion is that of I.M. Hutchings. Along with co-authors, he has produced a wealth of experimental data regarding erosion of brittle and ductile materials and far more relevantly on rubbers and elastomers (as discussed earlier in Section 2.1). Based on the know-how of their erosion experiments on rubber, Hutchings and co-authors presented analytical models for the erosion of rubbers at normal and at oblique incidences [8, 14]. Figure 2-11 shows the magnitude of erosion at normal incidence for different varieties of rubber. The following expression gives the erosion rate for normal incidence [14]:



$$\varepsilon = \frac{9\rho_t B}{100\rho_p R} \left( \frac{16\rho_p R (a\mu)^2 u^2}{3\pi(1-\nu^2)} \right)^\beta \quad (6)$$

Where,

R – particle radius

U – incident velocity

B,  $\beta$  – constants from tensile fatigue expts.

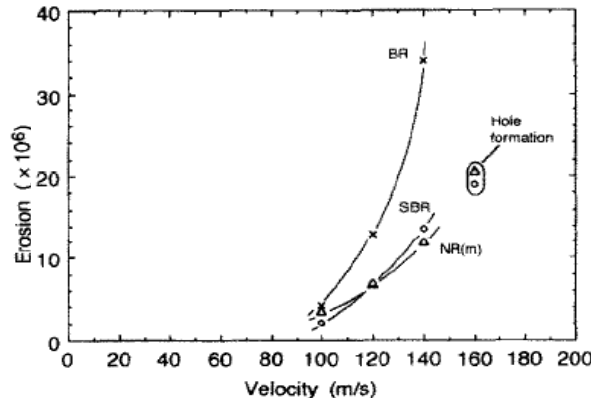


Figure 2-11 Variation of erosion rate in rubbers with increasing velocity under normal impact by sand [14]

The model for erosion of rubber at oblique impact angle is derived from the similarity of the wear characteristics with that of abrasive wear of rubber [8]. The following expressions give the erosion rate as compared to various incidence angles:

$$\varepsilon = \Phi \times \xi \quad \text{when } \mu \tan \alpha < 0.5 \quad (7)$$

$$\varepsilon = \Phi \times \zeta \quad \text{when } \mu \tan \alpha > 0.5 \quad (8)$$

where,

$$\Phi = 2 \left( \frac{8}{3\pi} \right)^{\frac{(\beta-1)}{2}} B \sin \theta (1 + \cos \theta)^\beta \times \rho_p^{\frac{(\beta-1)}{2}} u^{\beta+1} R^{\beta-1} \mu^\beta \rho_t \left( \frac{E}{1-\nu^2} \right)^{\frac{(\beta-1)}{2}} \quad (9)$$

$$\xi = \sin^\beta \alpha (\cos \alpha - \mu \sin \alpha) \quad (10)$$

$$\zeta = \frac{\pi^{\beta-1}}{2^\beta} \sin^\beta \alpha \left[ \cos \alpha - \mu \sin \alpha \left( 1 - \frac{\sin kt_c}{kt_c} \right) \right] \times kt_c \left( \frac{1 - \cos kt_c}{kt_c} \right)^\beta \quad (11)$$

$$kt_c = \cos^{-1} \left( 1 - \frac{1}{\mu \tan \alpha} \right) \quad (12)$$

R – particle radius

U – incident velocity

$\alpha$  - impact angle

$\theta$  – angle of cracks, approximately constant at 15 degrees

B, $\beta$  – calibrating constants (from tensile fatigue experiments)

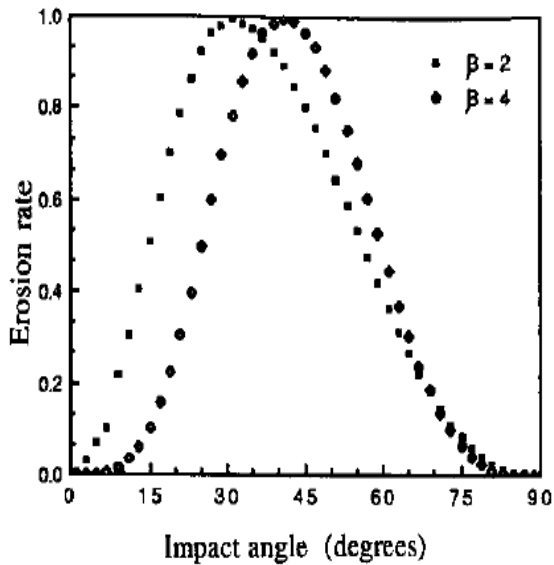


Figure 2-12 Predicted erosion rate for rubbers [8]

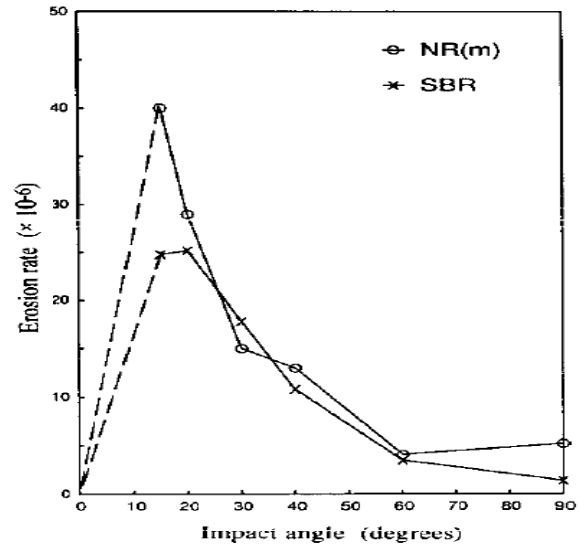


Figure 2-13 Measured erosion rate for rubbers [8]

As seen in Figure 2-12 and Figure 2-13 these models give good qualitative prediction (quantitative values being an order of magnitude higher) of erosion rates as they account for repeat-cycles of impact by the fatigue crack approach and large deformations (unlike Hertz contact mechanics) by using Boussinesq theory. Another advantageous aspect of these models being that the unknown constants in their relations can be found from tensile fatigue experiments thereby circumventing the need for erosion experiments to identify model parameters.

## 2.3. COMPUTATIONAL APPROACHES TO EROSION

Computational analysis of erosive wear has also seen gradual evolution as time has progressed. As for example, 2-dimensional plane strain or axisymmetric assumptions of impact have made way to full-scale 3 dimensional simulations, impact of a single particle - having been found inadequate for material removal – have made way to multi-particle repeated impacts at coincident or non-coincident locations. Some of these works are reviewed in the following section.

### 2.3.1. EROSION SIMULATION

Li et al. [15, 16] had used a Micro-Scale Dynamic Model to simulate material loss due to erosion of composites; Shimizu and Noguchi [17] performed single particle impact analysis on mild steel. Both of these analyses involved a plane strain assumption and although some of the erosion variables were discussed, no direct correlation was specified between these variables and the erosion parameters. Though the plane strain formulation of the problem is simple to implement, it is a misrepresentation of the erosion phenomena as it implies that a long cylindrical impactor is hitting the target. Thus the mass-loss or erosion rates obtained from these analyses can not be correlated to actual erosion data.

Griffin et al. performed 3d dynamic analysis of impact of 5 spherical particles on a Alumina scale-ductile substrate [18] and reported weight loss of the target as a function of erodent mass-flow and incident angle. Their simulation predicted that material loss doesn't happen at single impacts and requires a minimum of 3 co-incident impacts at low velocities; Figure 2-14 and Figure 2-15 depict these results.

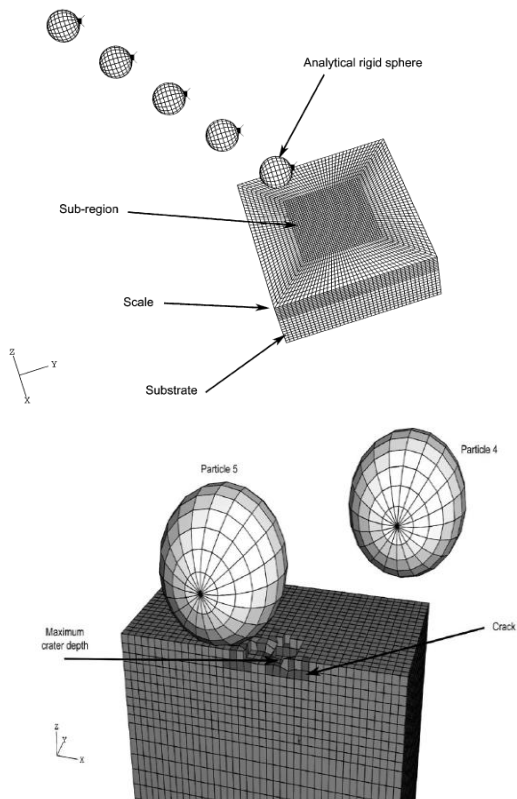


Figure 2-14 FEM model and eroded surface [18]

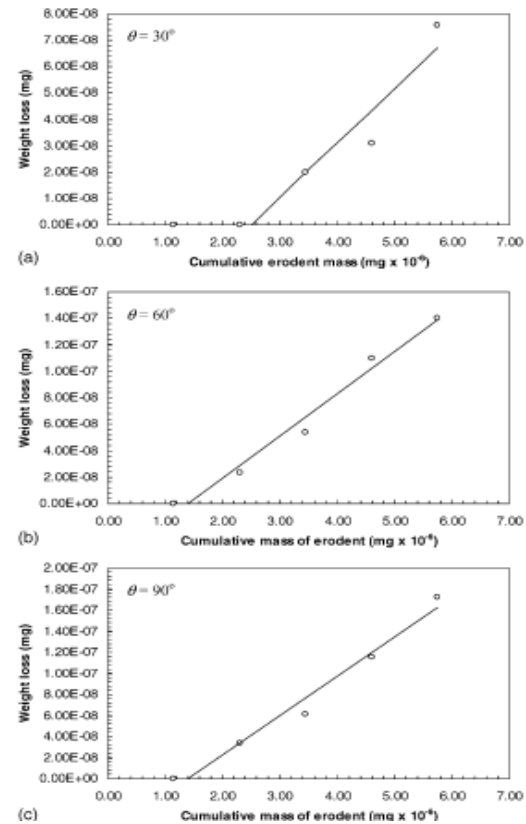


Figure 2-15 Weight loss vs. erodent mass flow [18]

ElTobgy et al. [19] performed similar explicit-dynamic analysis of solid particle erosion on Titanium and compared their predicted values with experimental data and predictions of prevalent analytical models. Figure 2-16 shows how their simulation results compares with select analytical models.

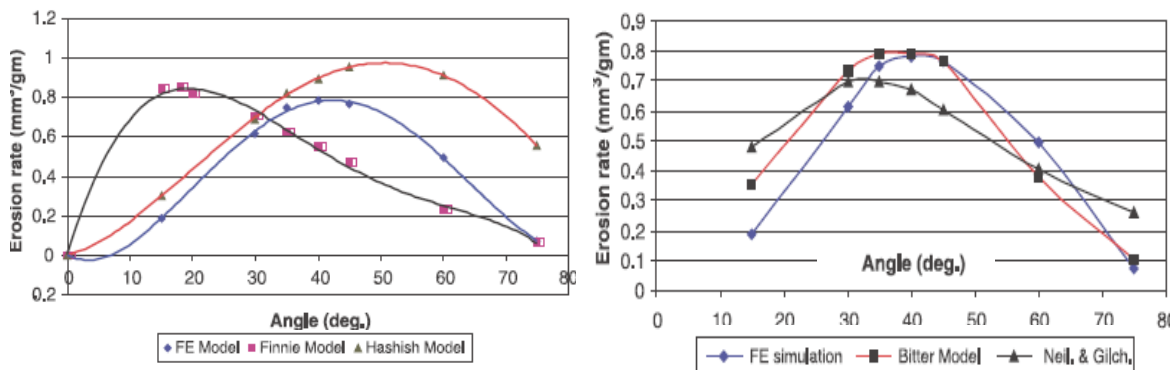


Figure 2-16 Erosion rate vs. incidence angle for ElTobgy [19] FE model and other analytical models

Woytowitz and Richman [20] and Wang and Yang [21] performed stochastic impact analysis where the impact sites were generated by a random-number generator. The first effort, in Dyna-3d dealt with impact of spherical particles on Copper targets and included three different damage accumulation techniques. It didn't include any material failure model and mass-lost couldn't be predicted. The deformation characteristics are presented in Figure 2-17.

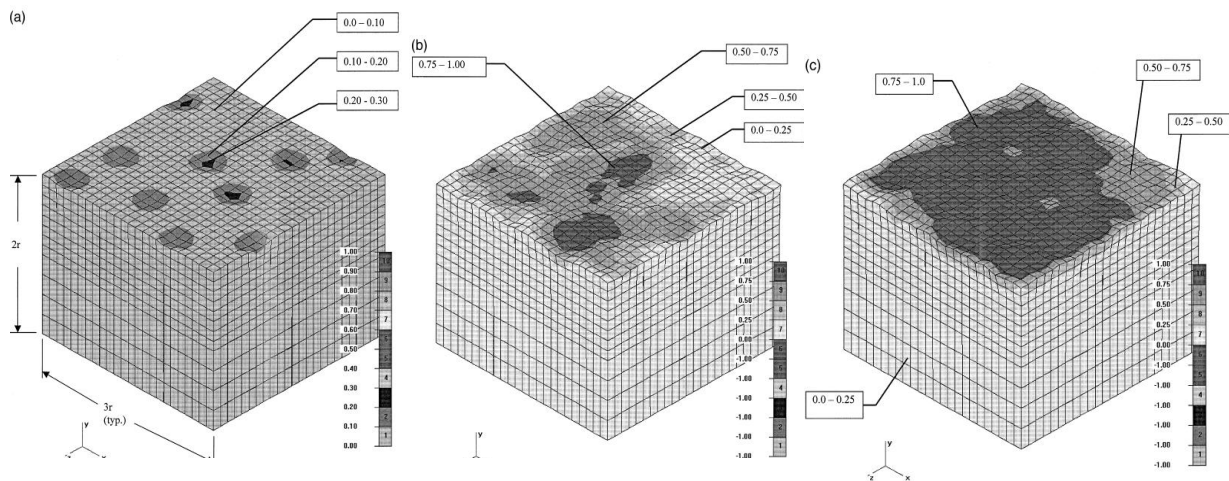


Figure 2-17 Deformed surface after non-coincident and stochastic impact 10, 100 and 200 particles [20]

The latter effort, by Wang and Yang, focused on both ductile (Ti) and brittle (SiC) targets with fracture criteria incorporated in the simulation and erosion mass loss was reported with respect to impact angles. Molinari and Ortiz [22] performed finite element simulations of the experiments of Hutchings et al. [23], consisting of high-strength steel spherical particles striking mild-steel target plates. The material description used in calculations for the target and the projectile included finite deformations, strain hardening, thermal softening, rate sensitivity, frictional contact, heat generation due to plastic working and friction, dynamics and heat conduction. The analysis provides insights into the relative roles played by plastic flow, friction and adiabatic shearing over medium to ballistic velocity ranges at normal to fully glancing impact.

### 2.3.2. MATERIAL MODELS USED IN SIMULATION

It is evident from the survey of literature that, so far, majority of the activities on erosion simulation has focused on ductile metallic or brittle ceramic targets. Accordingly, the material constitution employed in these analyses is restricted to the Johnson and Cook material model [18, 19, 24] with an associated tensile or shear failure criteria. An inhouse finite deformation plasticity model with temperature, pressure and rate sensitivity was used in [22] to model high strength steel. Seldom is any study reported on solid particle erosion of elastomeric materials. When it is, in a rare case, as in [25] where a removal of polyurethane (the material of relevance in this thesis) paint by solid particle impingement has been simulated, the same Johnson and Cook material model has been used to emulate the elastomer. In studies other than erosion simulation however, the instances of elastomeric materials being addressed is relatively higher. Dvorak and Bahei-El-Din [26], while studying the blast resistance of sandwich plates, used the Blatz Ko formulation to model a polyurethane interlayer as an isotropic nearly incompressible hyperelastic rubber material. Xue and Hutchinson [27], in an effort to study the necking in thin steel pressure vessels, found that substantial increases in necking limits and consequent energy absorption can be achieved for both quasi-static and dynamic stretching if an elastomer layer (PUR) was bonded to a metal layer. They employed a modification of the Mooney–Rivlin material to allow slight compressibility. [The Mooney-Rivlin material model is essentially non-linear elastic and cannot accrue the residual deformation due to plastic strain; an erosion process consists of multiple impacts where the target material is loaded (during initial contact), unloaded (during rebound) and reloaded (by subsequent impact) in a cyclic manner. Thus, to address erosion, atleast an elasto-plastic material model is a

necessity.] In a similar study, Nemat-Nasser et al. [28] addressed the failure resistance of steel plates to impulsive pressure loads, where the resistance was enhanced by spray casting a layer of polyurea on the back face of the plates. To model the polyurea, an experiment-based viscoelastic pressure and temperature sensitive model developed by Amirkhizi et al. [29] and implemented in LS-Dyna as an user-material subroutine was used. An aspect of these enhanced material descriptions is a time consuming parameter identification process. To circumvent this, Du Bois et al. [30] made a tabulated formulation of their strain-rate dependent hyperelastic material model with damage for rubber like materials [31] and performed a validation study of soft and hard rubbers under loading and subsequent unloading at different strain rates. This material model is available in the LS-Dyna models database.

Bergstrom and Boyce [32] formulated new micromechanism inspired constitutive model that allows for predictions of the large strain time-dependent behavior of elastomeric materials. The model is based on the assumption that the behavior can be decomposed into two networks acting in parallel: one network captures the equilibrium state and the second network gives the time-dependent deviation from equilibrium. The time dependence of the material is further assumed to be governed by the reptational motion of molecules that have sufficient freedom to change conformation during the loading. Furthermore, they incorporated these features into a large strain kinematics framework and the resulting constitutive model, whilst predicting rate, temperature and pressure sensitivity of polymers and elastomers as seen in experiments, became well suited for any arbitrary complex deformation and is available as a commercial user-subroutine to be incorporated into any finite element simulations code. To simplify the

seemingly complicated parameter identification process, a Matlab toolbox is provided with the commercial package where a range of experimental data can be easily fitted to generate the material parameters.

Another such versatile material model for polymers is the phenomenological model developed by Chowdhury et al. [33]. This so called macromolecular model accounts for pressure, rate and temperature sensitivity along with an orientation hardening characteristic of polymer networks. Being based on non-Gaussian networks, it is expected that this model can emulate the long chain behavior exhibited by elastomers like polyurethane. The formulation of this model and results pertaining to impact analysis of few glassy polymers are presented in Appendix A.

#### 2.4. LESSONS FROM LITERATURE SURVEY

Based on the literature survey, certain salient aspects of solid particle erosion can be summarized. The factors influencing Erosive Wear or the so called ‘Erosion Variables’ can be classified as shown in Table 2-1.

Table 2-1 Erosion variables

<b>ERODENT VARIABLES</b>	<b>FLOW VARIABLES</b>	<b>MATERIAL VARIABLES</b>
Particle Shape	Flow Velocity	Deformation
Particle Size	Angle of Impact	Damage
Particle Hardness	Mass Flux	Failure
	Impact Location	
	Particle Rotation	



The quantities through which the extent of erosion can be assessed, the so called ‘Erosion Parameters’ are as follows:

- Mass or Volume of Target Material Lost due to erosion
- Erosion rate (i.e. Mass Lost / Mass Flow of erodent)
- Size, i.e. width and depth of erosion crater
- Rebound Resilience (a measure of erosion resistance for rubbers)

Solid Particle Erosion involves three or more fundamental ‘levels’ of wear [13] Viz.:

- Deformation Wear
- Cutting Wear
- Fatigue Wear

Erosion experiments like sand blasting, media blasting etc, provides the best prediction of erosion rates and other erosion parameters thereby supplying engineers with the knowledge about the resistance and durability of protective coatings or surfaces (in general) when subjected to erosive environments. These experiments are, per se, time consuming, costly and cannot be performed in situ. Analytical models always come in handy in such situations. But, none of the prevalent erosion models could predict the solid particle erosion to acceptable quantitative or qualitative measures and those which approach some accuracy- do so by incorporating some calibrating constants – which necessitate some sort of extensive experimentation; it is highly unlikely that the situation would change in the future. The reasons might be that the models seldom account for all the ‘levels’ of wear in SPE [13] and/or that the erosion problem, with its many variables, is highly complicated, and that the simplifying assumptions in the models are compromising on the physics of the phenomena. The shortcomings notwithstanding, in

the long run, it would only be rational to attempt to formulate an analytical model that would give adequately accurate predictions of sand erosion of polyurethane elastomers. This can be achieved either by careful modification or manipulation of existing models or more preferably by starting from scratch by considering the material microstructure from the very onset.

That leaves the computational approach, which per se, can circumvent many of the constraints of experimentation or the limiting assumptions plaguing the analytical models. Fast computation capability enables virtual experiments in which all the erosion variables can be addressed in a controlled way and their effect on the erosion parameters determined and then compared with experiments. The review of erosion simulation literature revealed that so far, though many of the erosion variables have been accounted for in an isolated way in simulations, these activities have focused mostly on metals or ceramics and rarely on polymers or elastomers. Furthermore, particle shape [12] and rotation [34], two factors which have a crucial role in erosion but are often neglected [35] in modeling can be accounted for in simulations along with rubber-specific material models (for deformation and fracture) and the other erosion variables. It is possible that by performing simulations, one can grasp the underlying mechanisms of erosion, and also possibly acquire the material constants required for calibrating the analytical models thereby reducing the need for experimentation gradually.

### **3. PROBLEM FORMULATION**

#### **3.1. RESEARCH OBJECTIVE**

The objective of this study is to analyze, by means of computer simulation, the effect of erodent angularity on erosion severity of sand particle impact on polyurethane films. It is intended to achieve at least a qualitative prediction of the durability of these films against solid particle erosion which might enable us in the future to calculate the life of eroded films and their ability to shield the underlying titanium thereby allowing timely and cost-effective maintenance of the helicopter rotor blades.

#### **3.2. SIMULATION FRAMEWORK**

This section discusses the outlines of the simulation framework which has been employed in the study. The type of finite element analyses that has been performed has been explained along with the model geometries and boundary conditions invoked in the simulations. Furthermore, the material and fracture models employed in the analyses have been discussed briefly.

##### **3.2.1. TYPE OF ANALYSES**

An erosion process, in reality, consists of a randomly distributed set of erodent particles impinging on a target material. In this study, to represent the erosion process, the elastomeric target has been modeled as a film on a substrate which is impinged by a set of sand particles having a regular spacing as shown in Figure 3-1.

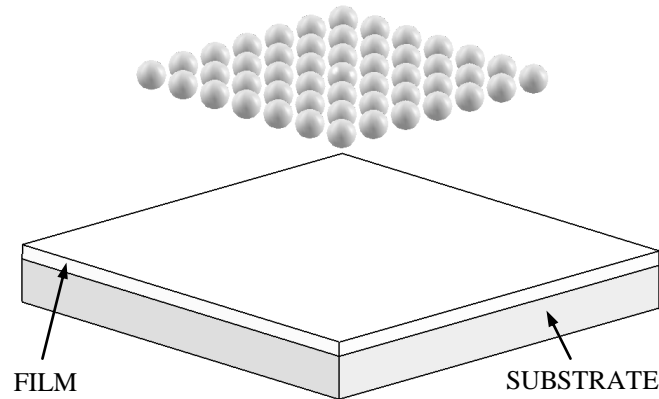


Figure 3-1 Target material impinged by erodent particles

Explicit dynamic finite element analyses were performed with the commercially available LS-Dyna software which performs a Lagrangian dynamic analysis using an explicit, central difference integration scheme. Two categories of analysis were performed. Firstly in a deformation analyses, the target was modeled without a material failure criterion and was impacted by erodent particles. Impact was simulated for different angularity and number of coincident hits. In another study, a material failure criterion was incorporated in the simulations allowing element deletion and thus, a quantitative measurement of mass lost due to erosion. This latter endeavor focused not only the angularity of erodents but also other erosion variables like velocity and angle of impact. Sections 5.1 and 5.2 are dedicated to the above studies.

To allow the contact interaction of the erodent (slave) with the target (master) the simulations employed a classical penalty based contact algorithm available in LS-Dyna as the `Contact_Automatic_option`. Options `Surface_to_Surface` and `Eroding_Surface_to_Surface` were used in the simulations without material failure and with it respectively. Contact interpenetration is often a problem in cases where there is a marked discrepancy in material properties of the master and slave surfaces. This being

the case for polyurethane and sand (see Section 4.1) a special segment-based option enabling '*soft*' contact was utilized in the simulations. For the same reasons a special hourglass control based on physical stabilization using an enhanced assumed strain method and with a performance similar to Belytschko-Bindeman [36] hourglass formulation has been incorporated in the analyses. More details on these implementations can be found in [37]. The following subsections deal with the details of model geometries, their finite element discretization, boundary conditions and material models used in the simulation.

### 3.2.2. MODEL GEOMETRY AND MESH

As mentioned in the previous section, the target PUR film has been modeled as a 3-dimensional square block mounted on a substrate. The substrate has not been explicitly modeled but added in the form of fixed boundary condition, more of which will be dealt with in the next sub-section.

Figure 3-2 shows a 3-d view of the PUR film with the characteristic dimensions labeled on it. The target PUR film has been modeled with eight-node brick elements with one integration point. Mesh grading has been used to reduce computation time and more importantly storage space. The characteristic dimensions are as follows:

$s$  = Length (and breadth) of PUR film (mm)

$s'$  = Length (and breadth) of ungraded zone (mm)

$h$  = Thickness of the PUR film (mm)

$e_b$  = Size of brick element in ungraded zone (mm)

These dimensions will vary in the different analyses; the exact dimensions will be separately mentioned at the beginning of the corresponding sections.

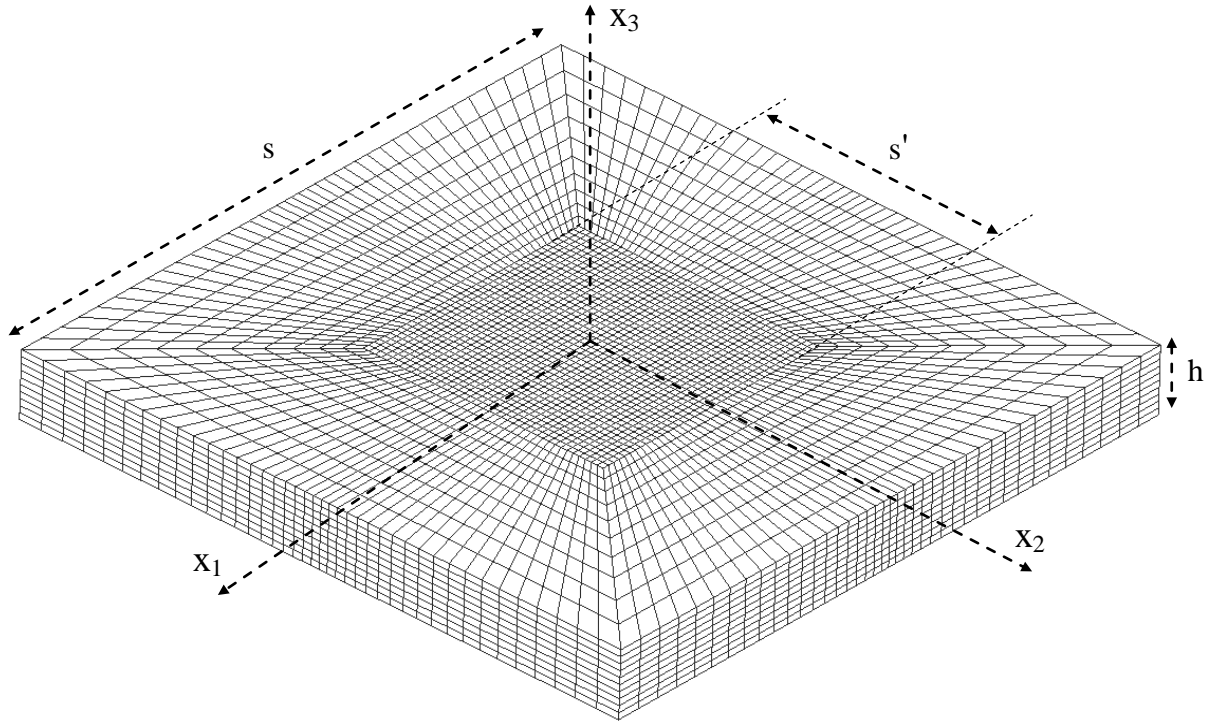


Figure 3-2 Target geometry showing finite element mesh with characteristic dimensions

In the simulations, two types of erodent geometries have been used, a spherical shape and an arbitrary angular shape. Both erodents have been modeled as a hollow shell with the intention of using a rigid-material constitution for silica sand. The spherical erodent has been discretized with 2-d four node plane stress elements whereas the angular one with a mix of three and four noded plane stress elements. The characteristic dimension of the angular erodent has been kept approximately same as that of the spherical erodent. Figure 3-3 shows the FE mesh of the spherical erodent and its diameter; Figure 3-4 shows the FE mesh of the angular erodent with its characteristic length and cutting point labeled in the figure.

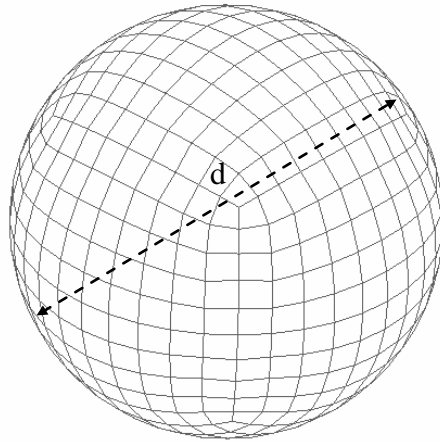


Figure 3-3 Finite element mesh of spherical erodent showing characteristic length

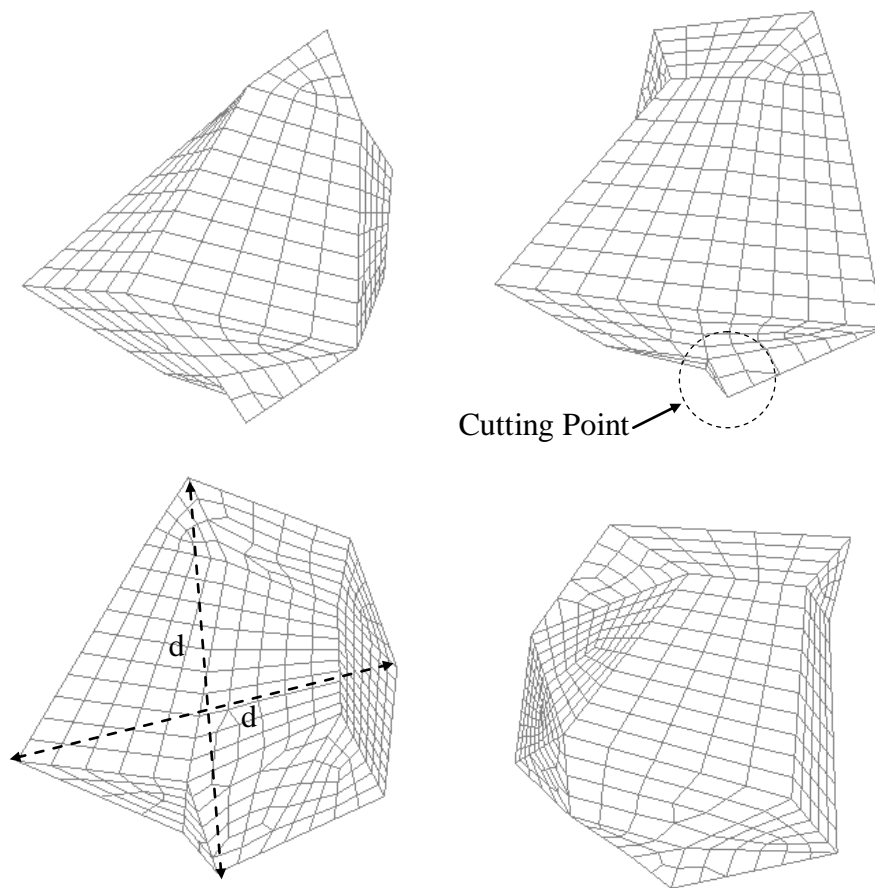


Figure 3-4 Finite element mesh and characteristic length of 'sharp erodent'. Four views showing faceted surfaces and cutting point from different perspectives.

All model geometries were created using the CATIA package. The finite element meshes were generated in the Hypermesh software which has unique mesh-manipulation controls and allows pre and post-processing for a number of FEA solvers. It was also used to apply boundary conditions on the target, which is the topic of the following sub-section.

### 3.2.3. BOUNDARY CONDITIONS

In this study the substrate has been emulated by incorporating a fixed boundary condition on the bottom face of the PUR film mesh (Figure 3-2). This boundary condition, as shown in Equation 13 also ensures that rigid body motion of the target is avoided. The impact is simulated by imparting a constant downward velocity, indicated by Equation 15 and 16, on the erodent particle. The term  $\alpha$  in those equations stand for the impingement angle measured from the horizontal.

$$u_1, u_2, u_3 = 0 \quad \text{for } x_3 = 0 \text{ and } |x_1|, |x_2| \leq s/2 \quad (13)$$

$$\text{Periodicity} \quad \text{on faces } x_1, x_2 = \pm s/2 \quad (14)$$

$$\dot{u}_3 = -V \sin \alpha \quad \text{vertical velocity component on the erodent} \quad (15)$$

$$\dot{u}_1 = -V \cos \alpha \quad \text{horizontal velocity component on the erodent} \quad (16)$$

Bi-directional periodic boundary condition is invoked on the lateral faces, as indicated in Equation 14. Three objectives are achieved by incorporation of the periodic boundary condition (PBC). The one which is most obvious is that the impact study of a regularly spaced set of erodent particles impinging on the target film (as shown in Figure 3-1) is simplified to studying just a unit-cell of the target being impacted by a single particle. Secondly, the PBC ensures that a geometric length-scale is introduced in the



simulation framework. Furthermore, this allowed a new descriptor of the angularity factor to be defined and included in the simulation.

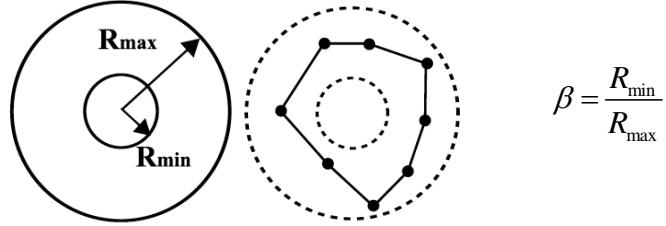


Figure 3-5 Annulus method for describing angularity

Figure 3-5 illustrates a prevalent scheme of describing angularity of arbitrary shapes. In this so called Annulus method a set of scattered points (the corners of an erodent) are confined within the limits of an annulus defined by a minimum radius ( $R_{min}$ ) and a maximum radius ( $R_{max}$ ). The ratio of these two radii, called  $\beta$ , describes the degree of angularity of the particle with the angularity or sharpness increasing as  $\beta$  decreases. This methodology enables us to indirectly invoke angularity into the simulation as follows.

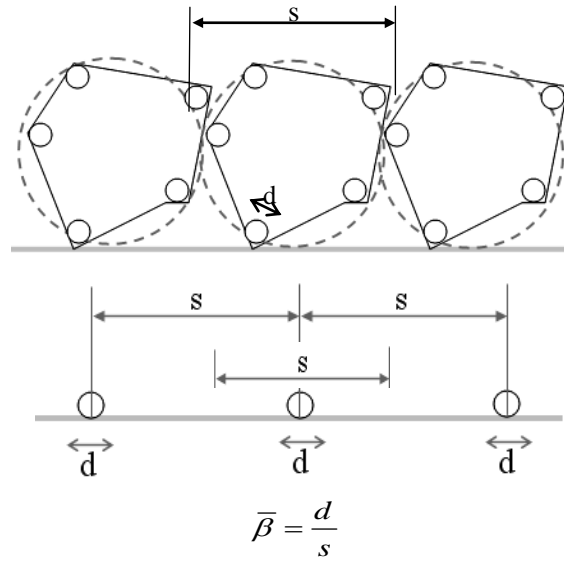


Figure 3-6 Periodicity and angularity description

It is frequently seen that even the sharpest of corners exhibit a corner radius; thus, the sharp corners can be approximated by incorporating a corner-radius as shown by the small circles of diameter ‘d’ in Figure 3-6. ‘d’ can be considered as a limiting case of  $R_{\min}$  as in the annulus method. The mass of the erodent is lumped at that corner by artificially scaling the density in the simulation. Furthermore, the spacing ‘s’ which in the densely packed limiting case is the size (like  $R_{\max}$  in the annulus method) if introduced as a normalizing parameter, the quantity ‘d/s’ gives an adequate representation of the angularity of the erodent with angularity increasing as d/s decreases. We call this new angularity descriptor as  $\bar{\beta}$ .

#### 3.2.4. MATERIAL MODELS

**Rigid Material Model for erodent:** Approximating a deformable body as rigid is a preferred modeling technique in many real world applications. This method is particularly suitable in this study as the target material (PUR) is much softer than the sand that impacts it. Elements which are assigned a rigid material are bypassed in the element processing and no storage is allocated for storing history variables; consequently, the rigid material model is very cost efficient. For this purpose, the erodent particles and their plane-stress elements were assigned the rigid material model (Mat\_20) in LS-Dyna.

**Elasto-plastic material model for PUR:** The thermomechanical behavior of polyurethane is complex and may be represented by any of the enriched material descriptions as mentioned in Section 2.3.2. However, in this study, the material is modeled using a simple elasto-plastic  $J_2$  flow theory employing a Von Mises yield criterion, associated flow-rule and isotropic hardening. This implementation, known as

Mat\_3 in LS-Dyna, follows a simplification of the constitution developed by Krieg and Key [38] the salient aspects of which are as follows:

The yield function is:

$$\phi = \frac{3}{2} s_{ij} s_{ij} - \sigma_y^2 = 0 \quad (17)$$

$s_{ij}$  and  $\sigma_y$  being the stress deviator and the yield stress respectively

The rate of deformation is decomposed into an elastic part  $D^e$  and a plastic part  $D^p$ .

Where, the elastic part of the response is expressed by a hypoelastic law in terms of the Jaumann derivative [37] and the plastic part is expressed as the following flow rule:

$$D_{ij}^p = \lambda \frac{\partial \phi}{\partial \sigma_{ij}} \quad (18)$$

$\lambda$  being the plastic multiplier

The Hardening Law is:

$$\sigma_y = \sigma_y^0 + E_p \varepsilon_{eff}^p \quad (19)$$

where

The plastic hardening modulus is:

$$E_p = \frac{E_t E}{E - E_t} \quad (20)$$

And effective plastic strain is:

$$\varepsilon_{eff}^p = \int_0^t \left( \frac{2}{3} D_{ij}^p D_{ij}^p \right)^{\frac{1}{2}} dt \quad (21)$$

### 3.2.5. FRACTURE MODEL

Quantification of mass lost due to erosion requires a fracture criterion to be included in the simulation framework. In the simulations as described in section 5.2 a fracture criterion is invoked and material failure happens when the volume averaged equivalent stress levels in the impact zone reaches a user specified critical value. The failure criterion is written as:

$$\bar{\sigma}_{eq} \geq \sigma_c \quad (22)$$

where the volume averaged equivalent stress is

$$\bar{\sigma}_{eq} = \frac{1}{V} \int_V \sigma_{eq} dV \quad (23)$$

where  $V = V_e$  is the elementary volume over which the erosion process takes place at the microstructural scale (section 5.2.1);

and the von Mises equivalent stress being given by

$$\sigma_{eq} = \sqrt{\frac{3}{2} s_{ij} s_{ij}} \quad (24)$$

## 4. MATERIAL PARAMETER IDENTIFICATION

### 4.1. DEFORMATION

Sand: Though the erodents (sand) has been modeled with a rigid material constitution, Young's modulus and Poisson's ratio are used for determining sliding interface parameters if the rigid body interacts in a contact definition; hence, realistic values for these constants were needed to be defined since unrealistic values could have contributed to numerical problems in contact. The material parameters used for sand are shown in Table 4-1.

Polyurethane: The macroscopic response of polyurethane is similar to typical thermoplastic elastomers exhibiting almost no post-yield softening and deformations till very large strain without fracture. Figure 4-1 shows the stress – strain response of PUR thin films under uniaxial tension at room temperature for different strain rates. Figure 4-2 shows the bi-linear stress-strain curve of the elasto-plastic material model being employed in the simulation, superimposed on the PUR macroscopic response and the good correlation, atleast for the forward loading portion shows that the elasto-plastic approximation has sufficient merit considering the scope of this endeavor. The list of material parameters used in simulation for PUR has been shown in Table 4-1.

Admittedly, the unloading response and other characteristics of PUR behavior, like temperature, rate, pressure sensitivity, cannot be captured by the elastoplastic material model. There are other enriched material constitutions, many of which have been cited in section 2.3.2, which can address these issues; furthermore, a preliminary study with one of the most advanced of these models has been presented in Appendix A.

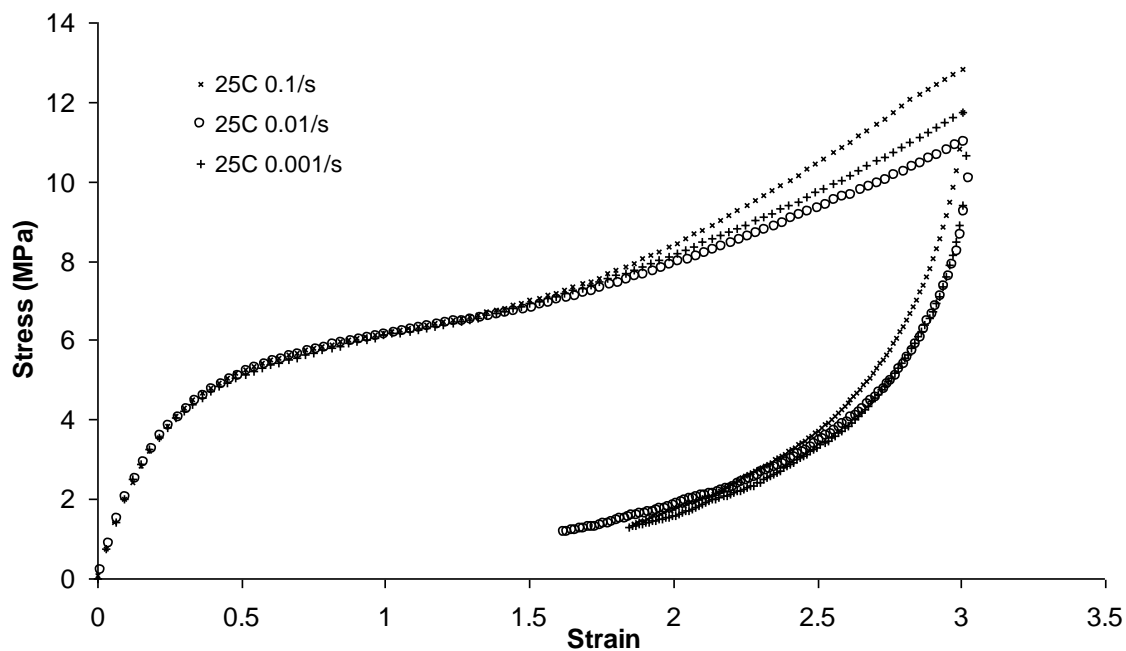


Figure 4-1 Stress - strain response of PUR thin film under uniaxial tension

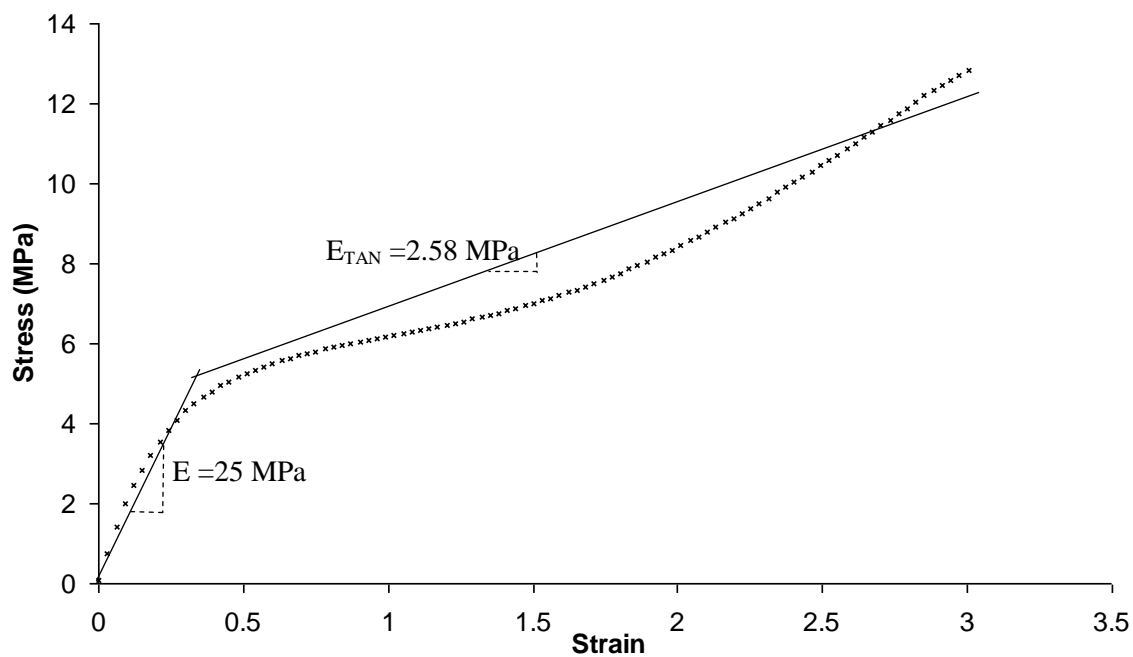


Figure 4-2 Elasto-plastic approximation of PUR macroscopic behavior

Table 4-1 Material parameters used in simulation

(Source: MATWEB online resource and uniaxial tension test on PUR)

<b>SI-mm unit convention</b>	<b>Polyurethane</b>	<b>Sand</b>
Density, $\rho$ (tonne /mm <sup>3</sup> )	1.12 e-09	2.63 e-09
Young's Modulus, E (MPa)	25	68, 000
Poisson's Ratio, $\nu$	0.25	0.19
Yield Stress, $\sigma_y$ (MPa)	7.68	
Tangent Modulus, $E_{TAN}$ (MPa)	2.58	
Static friction coefficient, $f_s$	0.1	

#### 4.2. FRACTURE

Estimating the fracture parameters of PUR was not as straight forward because of two reasons. Firstly, there is a serious dearth of literature regarding fracture tests of PUR. Secondly, conducting experiments to determine the fracture parameters was not possible with the thin films of PUR that was available for limited mechanical testing. Estimation of fracture parameters requires bulk material (not films) to construct notched specimens which can give very credible and comprehensive fracture data. In the absence of this, the thin films were subjected to uniaxial tensile load till fracture. The material failed at quite high strains, not due to actual fracture but due to localization near the grips of the tensile test apparatus. The maximum stress at failure not being representative of the true fracture stress, a workable solution was obtained by using the peak stress, shown in Figure 4-3 to be 15 MPa (for the higher strain rate), and performing the failure analysis (section 5.2) by invoking the critical stress as a parametric reduction of this peak value.

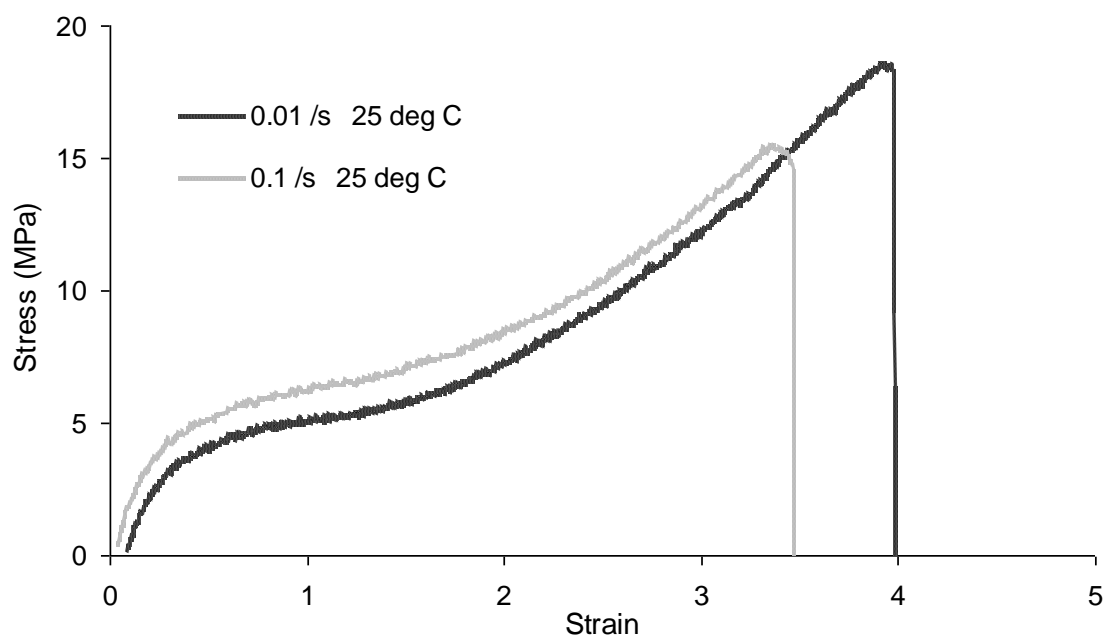


Figure 4-3 PUR tensile test till fracture



## 5. RESULTS AND DISCUSSION

### 5.1. DEFORMATION ANALYSIS

Computational impact analysis has been performed on the PUR block subjected to vertical impact by the spherical impact. The purpose of this study was to illustrate the effect of angularity on erosion. Admittedly, material fracture is a necessity to quantify erosion but deformation precedes fracture and it was anticipated that this would give a good qualitative estimate of the effect of angularity. Molinari and Ortiz [22] performed similar impact analysis, albeit on steel, and provided geometrical details of the erosion crater. It won't be out of place to recall here that 'crater geometry' is a listed erosion parameter [Table 2-1] and is an adequate quantity to estimate the magnitude of erosion that would occur if and when material fracture is incorporated into the simulation framework [Section 5.2].

The details of the FE mesh used in these simulations are (according to conventions specified in Section 3.2.2):

$$s = s' = 10\text{mm}$$

$$h = 1\text{mm}$$

$$e_b = 0.1\text{mm}$$

$$d = 1\text{mm}, 3\text{mm}, 5\text{mm}$$

The first condition implies that the mesh was not graded in these analyses because of reasonable runtimes. The diameter of the spherical erodent was varied from 1 to 3 mm thereby yielding effective angularities (given by  $d/s$ ) of 0.1, 0.3 and 0.5 (according to section 3.2.3) with the least value corresponding to the sharpest case. Also, the densities of the rigid material of these spherical erodents were scaled to match a 1mm grain of

sand, so that in each case the mass of the erodent and hence the kinetic energy imparted onto the target was same. Boundary conditions were same as mentioned in (section 3.2.3) with  $\alpha$  in equations 15 and 16 being equal to  $90^\circ$ , yielding the effective impact velocity as  $-V$ . To estimate the magnitude of the impact velocity, the concept of threshold velocity (equation 3) of the Bitter's model [1] was used.

The threshold velocity is that, which if exceeded, will result in the material yielding under the impact zone. With the material parameters listed in section 4.1, equation 3 predicts a threshold velocity of 8.5 and 26.8 m/s (for the two values of  $\sigma_y$ ), whereas the simulations predicted 24.5 m/s and 47 m/s indicating that Bitter's equation was over-predicting the erosion criteria. As such, to study the effect of angularity in the simulations, an impact velocity of 50 m/s was employed in these simulations. Thus,  $V = 50000$  mm/s (adhering to the consistent set of units of the SI-mm convention)

The analysis also emulated multi-particle co-incident impact. To achieve this, instead of explicitly including  $n$ -number of particle-models into the simulation, the density of one particle was scaled by  $n$  to simulate the  $n^{\text{th}}$  impact. This approach is sufficient in this case where only deformation analysis is being performed using an elasto-plastic material model. The residual plastic deformation after  $n$  impacts is not a function of time and so it would not matter if all the kinetic energy is dumped at once. However, if a visco-plastic constitution were used for the target and / or a stress-based fracture criterion to simulate material failure, then the timescale of the dynamic process of solid particle impact and consequent erosion would have had to be taken into account. This has been done in section 5.2 where erosion mass loss has been quantified using a stress-based fracture criteria.

Figure 5-1 shows the iso-surfaces of contours of the plastic strain under the impact zone after five vertical impacts as accumulated due to hits by erodents of different angularity. It is evident from this figure that the amount of plastic strain is maximum when the sharpest erodent ( $d/s$  0.1) impacts the target and substantially lower as the sharpness (or angularity) reduces to 0.3 and 0.5. It can also be observed that in the case of the less sharp erodents (i.e.  $d/s$  0.3 and 0.5) the zone of plasticity lies away from the surface and inside the bulk of the target material. One obvious cause of this phenomenon are the fixed boundary conditions near the bottom face; in addition, one can draw an analogy to tensile tests using notched specimens where it is frequently seen that for shallow notches the zone of plasticity develops at the center and progresses to the surface of the notch at a slower pace than it does in the case of a sharp notch. This happens because of the triaxiality of stresses which is a strongly decreasing function of position from the midsection of these specimens. In the impact scenario, we can compare the instantaneous deformation caused by the sharp particle to a sharp notch and that by the blunt particles to shallow notches; and the resulting triaxialities lead to the development of the plastic zone internally in the target. This zone would, obviously, progress to meet the surface of the impact crater after further impacts.

Figure 5-2 shows the time history of the plastic strain for all the test cases. It can be seen that for the least sharp particle ( $d/s$  0.5) no plastic strain is accumulated till at least 5 impacts were registered and even after that the amount of plastic strain is quite negligible as shown also in Figure 5-1(a). These varying magnitudes of the plastic strain in the different cases entail that the residual deformation under the impact location will differ; this is shown in Figure 5-3 which gives a lateral perspective of the impact craters. Clearly

the severity of impact (as seen from the depth of deformation) is much higher for the sharpest particle as compared to the relatively blunt ones. To correlate these results to viable erosion parameters, the crater geometry is approximated as a spherical cap whose volume is given by:

$$V = \frac{\pi b(3a^2 + b^2)}{6} \quad (25)$$

where,  $a$  and  $b$  are the radius and depth respectively of the spherical-cap.

Applying Eqn.23 to the results, we obtain the crater volume under the impact zone which when plotted against the angularity ( $d/s$ ) yields the curve in Figure 5-4.

Figure 5-4 clearly shows that as  $d/s$  decreases i.e. angularity increases the crater volume progressively increases and that atleast 5 coincident impacts are necessary for the bluntest erodent to cause any residual deformation under the impact zone. Figure 5-4 is the first example, in known erosion literature, which captures, from computer simulation, such a trend of erosion severity of any angularity parameter.

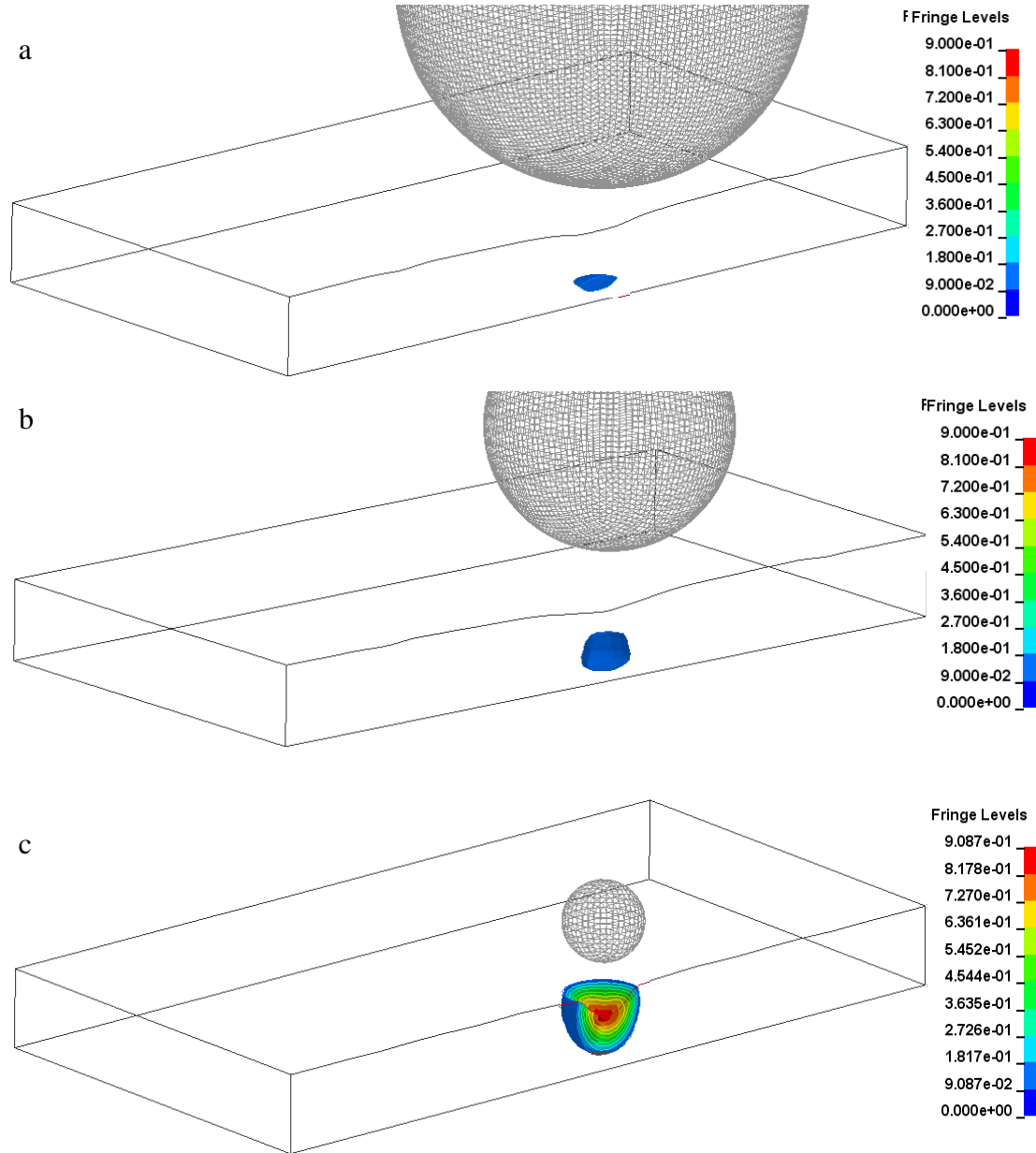


Figure 5-1 Iso-surfaces of contours of plastic strain after 5 vertical impacts at 50m/s. Colored contours indicate the intensity of plastic deformation with erodents of different angularity  $d/s$  (a) 0.5, (b) 0.3, (c) 0.1. One half of the target mesh has been masked for the sake of clarity in viewing the contours.

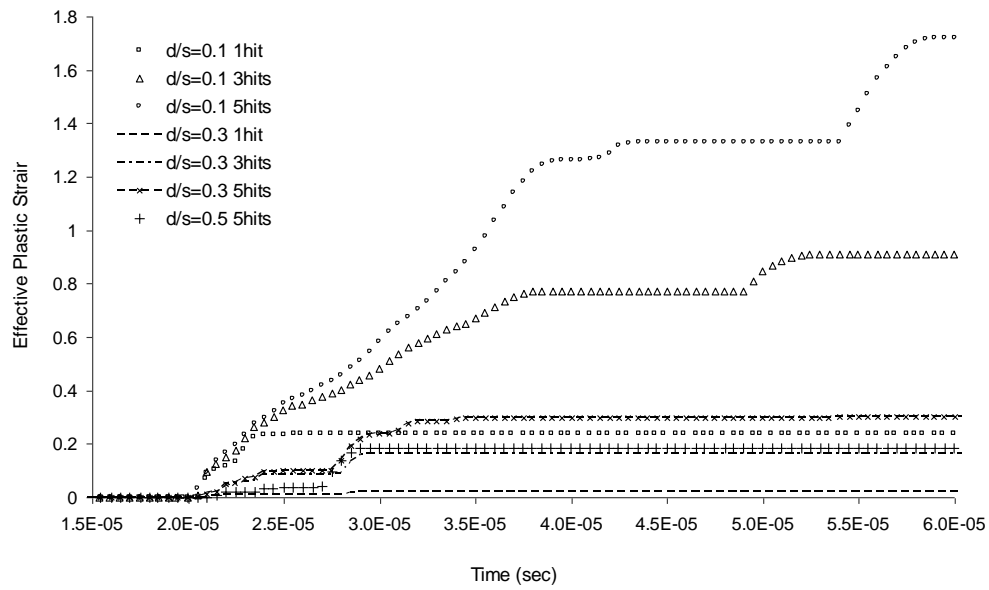


Figure 5-2 Time history of plastic strain for different angularities and multiple impacts

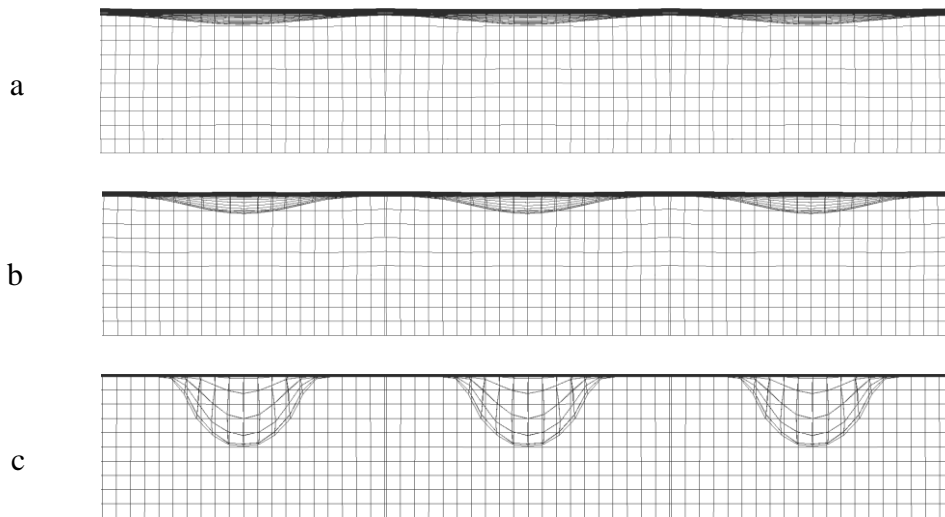


Figure 5-3 Side view of deformed target after 5 coincident hits.  
Angularity  $d/s$  (a) 0.5, (b) 0.3, (c) 0.1

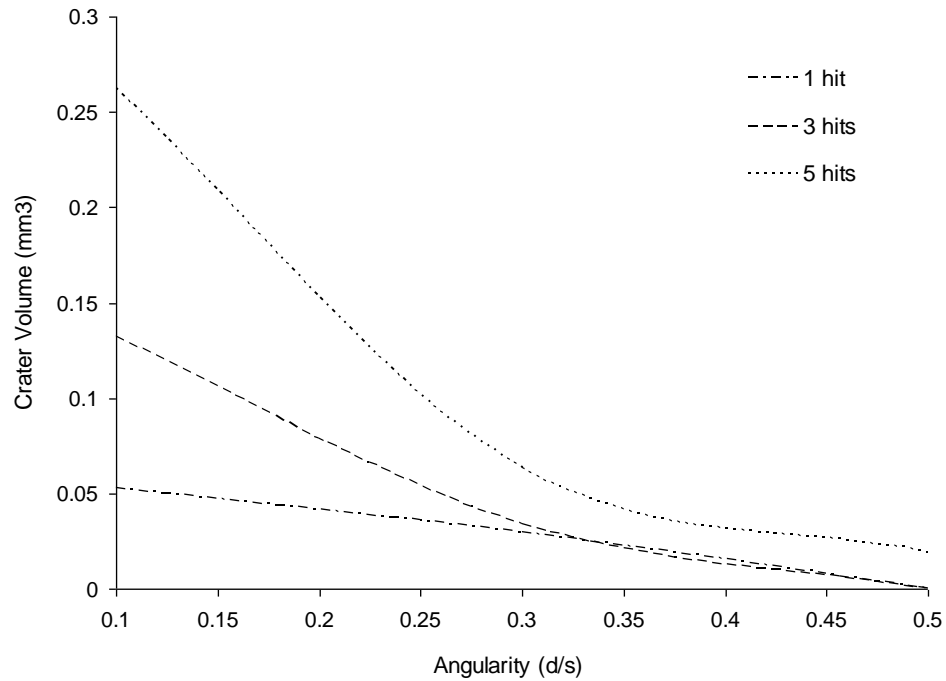


Figure 5-4 Effect of angularity on volume of impact crater

The present results provide an initial and quite adequate qualitative estimate of the extent of erosion that might occur if damage is driven by deformation and plasticity under the impact zone. The section that follows deals with the scenario where, by introducing an appropriate fracture criterion, the mass lost due to erosion has been quantified.

## 5.2. FAILURE ANALYSIS

This section deals with the analyses which aim at quantifying the mass lost due to erosion by incorporating the fracture criterion as discussed in section 3.2.5 into the simulation framework. The section is further divided into two sub-sections, one dealing with impact by spherical erodents (with the d/s angularity description), and another dealing with the impact by the discretely modeled sharp erodent of Figure 3-4. In both cases simulations have been performed for full range of impact angles starting from vertical to as low as 20 degrees.

### 5.2.1. IMPACT WITH SPHERICAL ERODENTS

The details of the FE mesh used in these simulations are (according to conventions specified in Section 3.2.2):

$$s = 10\text{mm}$$

$$s' = 4\text{mm}$$

$$h = 1\text{mm}$$

$$e_b = 0.05\text{mm}$$

$$d = 1\text{mm}, 3\text{mm}, 5\text{mm}$$

$$V = 50, 75, 100, 125, 150 \text{ m/s}$$

The element size has been reduced to 50 micron to be of a length-scale comparable to that of the microstructural details of PUR as seen in Tocha et. al. [39]. The PUR microstructure exhibits globules and spherulites (hard-segments) in a matrix like phase (soft-segment). The diameter of these spherulites can be of the order of 15-20 microns and this was the justification for selecting the element size of the same order since cracks in the PUR material propagates through the soft segments.



To quantify the erosion mass loss, the fracture criterion mentioned in section 3.2.5 has been invoked in the simulation. Erosion severity has been studied parametrically by varying the impact velocity and angularity and also the critical stress required for failure (section 4.2). Before this endeavor was undertaken, a sanity check was performed by running analysis with the critical stress (for failure) set to values lower than the yield stress, nearly equal to the yield stress and higher than the yield stress. The simulations predicted lowest material removal for the last case where the critical stress was reached after certain hardening of the material; for the case with critical stress set nearly equal to the yield, more material failed because the failure was forced to happen as soon as the material yielded. Maximum material failure occurred in the case with critical stress set below the yield; this was anticipated as the imposed condition implied a brittle fracture criterion. This academic study substantiated the credibility of the simulation framework.

For the actual test-cases, multiple co-incident impacts have been simulated, not by scaling the density, but by discretely modeling  $n$  different erodent particles for  $n$  impacts ( $n = 3$ ). The reason for discretely modeling the erodents lies in the inherent time-scale dependence of the dynamic process of impact and material failure on attainment of a critical stress. This is well illustrated by Figure 5-5 and Figure 5-6 which show the time history of impact for impact by a spherical erodent of  $d/s$  0.3 at velocities 50 m/s and 125 m/s respectively. The critical effective stress for these simulations was 12.5 MPa.

Figure 5-5 (a) shows the variation of impact velocity for the 3 impacts. An initial velocity of 50 m/s (negative because of the downward direction) is imparted on the first particle which makes contact with the target at around 20  $\mu$ s and starts a gradual upward rebound as shown by the rebound velocity profile which become positive. Sufficient time

is allowed for the particle to lose contact with the target completely during rebound before it is removed from the simulation and the 2<sup>nd</sup> particle is introduced at around 40  $\mu$ s. Figure 5-5 (a) shows how a gradual ramp is applied to enable the 2<sup>nd</sup> particle reach the same impact velocity of 50 m/s; the 2<sup>nd</sup> particle contacts the target at around 65  $\mu$ s and then starts the gradual rebound. This cycle continues for the 3<sup>rd</sup> particle as well. Figure 5-5 (b) shows the global time history of effective stress for the same simulation. The stress peaks attained after each of the three impacts has been labeled in the figure. The dynamic nature of the impact problem is clearly evident in the fluctuations of the stress levels. It can be noted that after the peaks the stress levels gradually tend to decrease. This decay would have continued had not the subsequent impact caused another peak. It is interesting to note that had the next impact occurred after considerable duration of time has been allowed for the stresses to completely die out, the peaks would have essentially been of same magnitude (allowing a certain tolerance to this hypothesis based on the dynamic nature of the problem). In the simulations of these virtual impact scenarios the duration between subsequent impacts has been maintained at around 45  $\mu$ s (thereby preventing a complete decay of stress levels in the PUR target) to permit the peak stresses to intensify with successive impacts. Figure 5-5 (b) shows that for the impact with an erodent of angularity  $d/s$  0.3 at 50 m/s, the critical stress of 12.5 MPa is not reached. However, the same limit has been reached when the impact velocity is 125 m/s as shown in Figure 5-6. Figure 5-6 (b) shows that after the 3<sup>rd</sup> impact the stress peak breaches the threshold set by the critical stress and causes material failure (elements that meet the fracture criteria are deleted) thereby enabling quantification of mass lost due to erosion. Also, signature of the material failure shows up in Figure 5-6 (a) where the rebound

velocity after the 3<sup>rd</sup> impact is visibly lower than the previous two; this can be attributed to the dissipation of energy due to fracture.

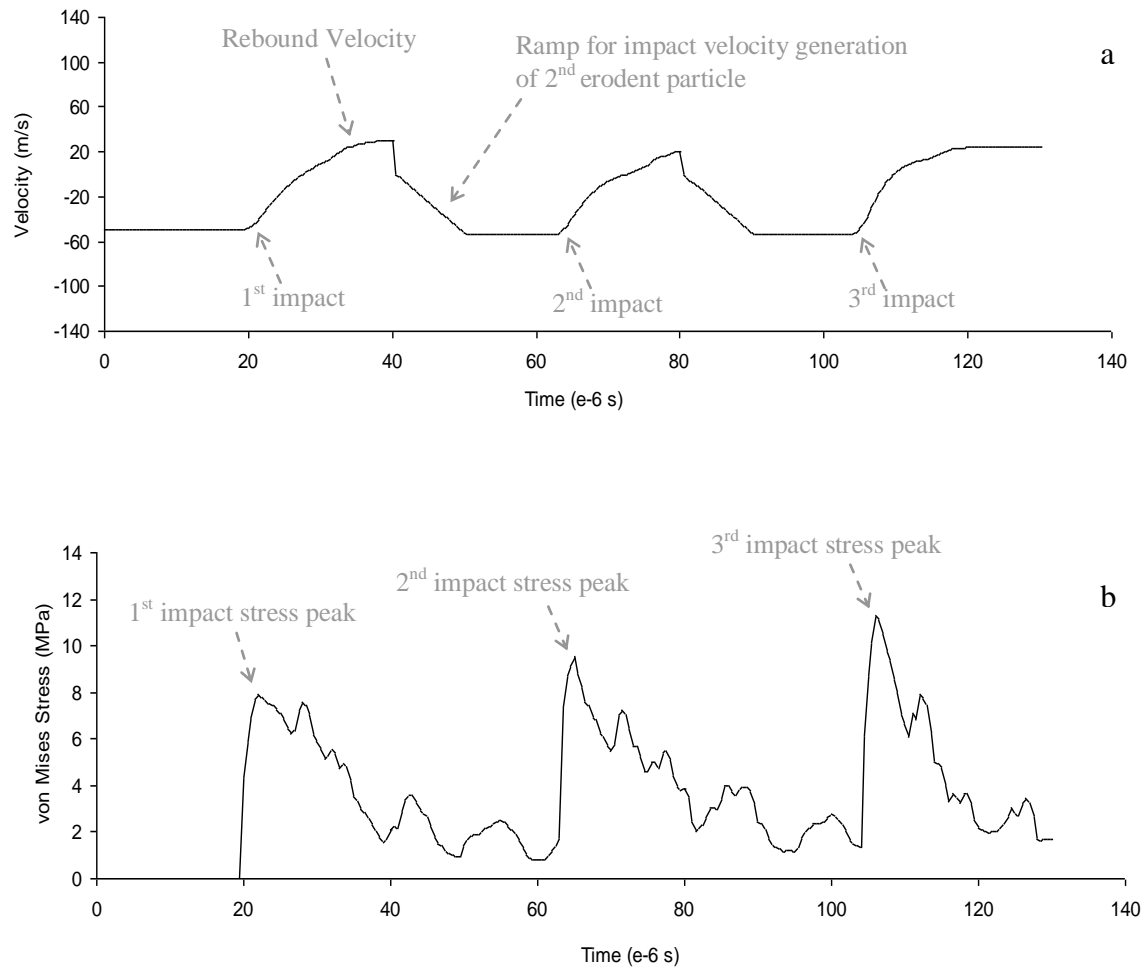


Figure 5-5 Impact at 50 m/s with d/s 0.3 and critical stress 12.5 MPa.  
(a) time history of velocity and (b) time history of effective stress.

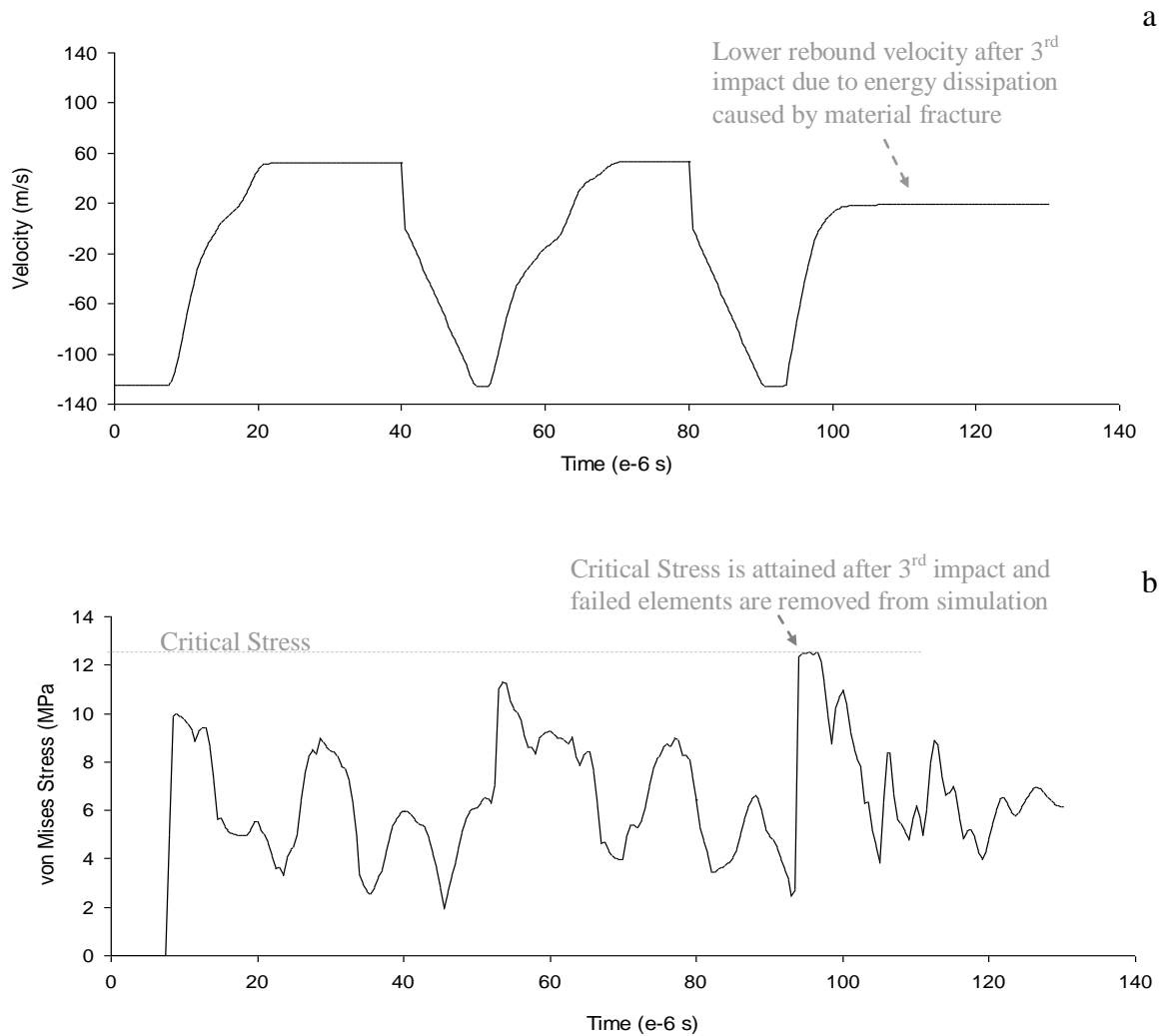


Figure 5-6 Impact at 125 m/s with  $d/s$  0.3 and critical stress 12.5 MPa.  
 (a) time history of velocity and (b) time history of effective stress.

Figure 5-7 shows the topography of the PUR target after erosion caused by material failure (and element deletion) for impact at 125 m/s with an erodent of angularity  $d/s$  0.3.

For few of the more severe impact cases the erosion severity was high enough to remove almost all the material under the impact zone meaning that the protective-capability of the PUR coat would have been lost and any subsequent impact at the same location would have affected the titanium substrate (had it been discretely modeled in the simulations). In some case, as shown in Figure 5-8 the erodent can be captured in the crater formed at the eroded impact zone. Figure 5-8 (b) is an SEM showing a spherical impactor embedded in a PUR film eroded at 150 m/s and 90 degrees; Figure 5-8 (a) is the output from simulation which shows good match with the experimental observation.

To calculate the exact amount of material lost due to erosion, the number of elements deleted has been multiplied with the mass of one element (in the graded zone). Figure 5-9 through Figure 5-12 shows the trends of the mass loss with respect to velocity and angularity for few of the test cases. Figure 5-9 compares the erosion magnitude for successive impacts at fixed angularity of 0.1 for velocities ranging from 50 to 150 m/s. It can be observed that a single hit at 50 m/s was not sufficient to cause erosion; also the plot shows same mass loss for 2<sup>nd</sup> and 3<sup>rd</sup> hits at 125 m/s and 150 m/s because all the material under the impact zone was eroded after the 2<sup>nd</sup> hit thereby leaving nothing to be eroded during the 3<sup>rd</sup> impact. Figure 5-10 compares the erosion magnitude after 2 impacts by erodents of different angularity for velocities ranging from 50 to 150 m/s and shows that no erosion is registered for the blunt particles,  $d/s$  0.3 and 0.5, for velocities lesser than 75 m/s and 100 m/s respectively. Figure 5-11 and Figure 5-12 shows the variation of

erosion mass loss with respect to angularity for different velocities and different number of hits respectively and complements Figure 5-4.

Figure 5-13 shows a set of comprehensive histograms which encompass the results from all of the 180 test cases (i.e. 5 velocities, 3 angularities, upto 3 co-incident impacts and parametric study with 4 different critical stresses). Such histograms can be quite useful to engineers to evaluate the life and durability of protective coats subjected to erosion.

So far, results have been presented for perpendicular impact with spherical particles. The results show good match with the trends reported in literature for perpendicular impact. But, when the same methodology was employed to simulate inclined impact, the erosion curve obtained from simulation deviated from those observed in literature. Figure 5-14 shows the mass loss as a function of angle of impact. Clearly the mass loss progressively increases from glancing impact to normal impact. However, it is an established fact that the erosion curves for elastomers (also ductile materials) exhibit maxima at low impact angles, as reported earlier in Figure 2-13 (and Figure 2-10).

The reason for such a deviation can be explained by comparing the simulations to the reality and probing deeper into the mechanisms of erosion. Figure 5-15 shows a snapshot of a simulation where the impact was by the sharpest ( $d/s$  0.1) erodent incident at an angle of  $30^\circ$  with a velocity of 150 m/s. The inclination entails that the impact velocity is resolved into two components; the horizontal component leads to sliding and the vertical component, now reduced in magnitude, doesn't impart enough energy to breach the threshold and cause deformation; hence the absence of plastic strain or residual deformation in Figure 5-15. Note that the rebound angle is lesser than the incident angle.

This is because of a slight loss of impact energy due to friction between the erodent (sand) and target (PUR).

Thus, a mono-particle impact was insufficient to cause erosion and actually even after 5 inclined impacts the threshold was not breached. It would not be out of place to mention here that a ‘literature re-survey’ regarding erosion of soft and ductile targets at inclined angles revealed that most of the reported data corresponds to erosion by sand or abrasives and never by spherical beads. There is clearly a dearth of appropriate experimental data to compare the above simulation results with. However, it is believed that the mechanisms of erosion are predominantly deformation driven, and so it can be anticipated that if a multitude of impacts can be simulated (like in an eroding environment in reality) then the fatigue mechanisms would ensure that at some point in time the threshold is breached and mass loss occurred, and possibly capture the maxima at lower angles. Because such large scale simulations were beyond the scope of this endeavor, it was decided to study the erosion effect of the discretely modeled sharp erodent (Figure 3-4) with the intuition that the sharp cutting point would accelerate the erosion mechanisms by causing very high local stresses at the point of contact. The subsection that follows deals discusses the simulations performed with the sharp erodent.

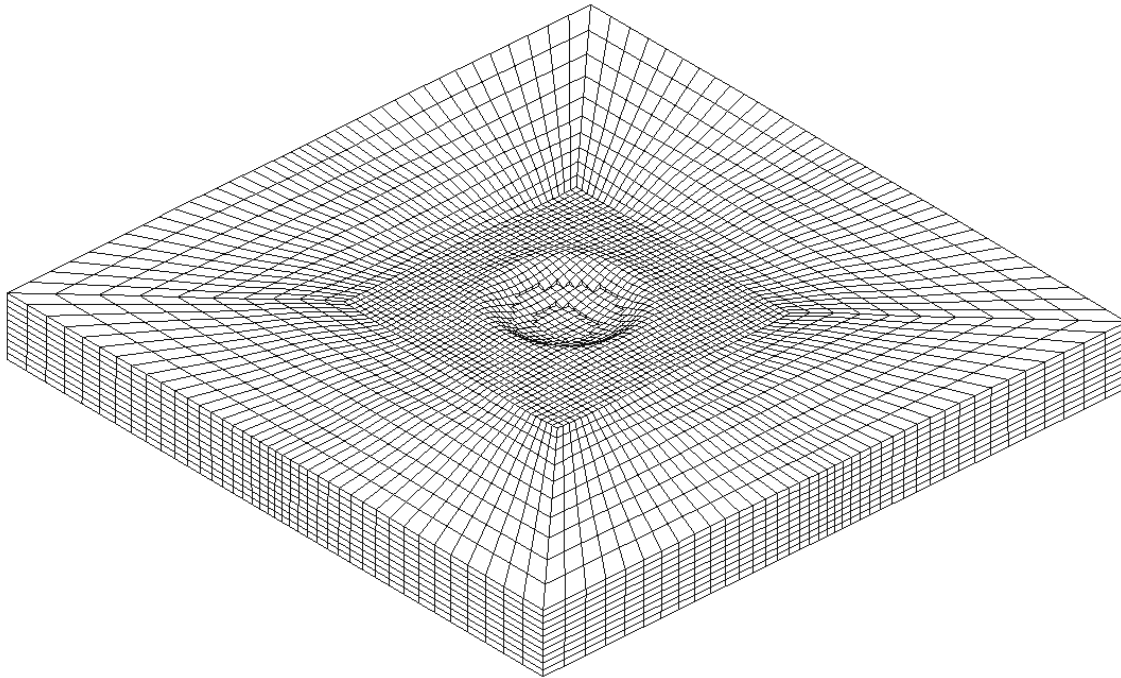


Figure 5-7 Topography of eroded PUR target after impact at 125 m/s by d/s 0.3 spherical erodent

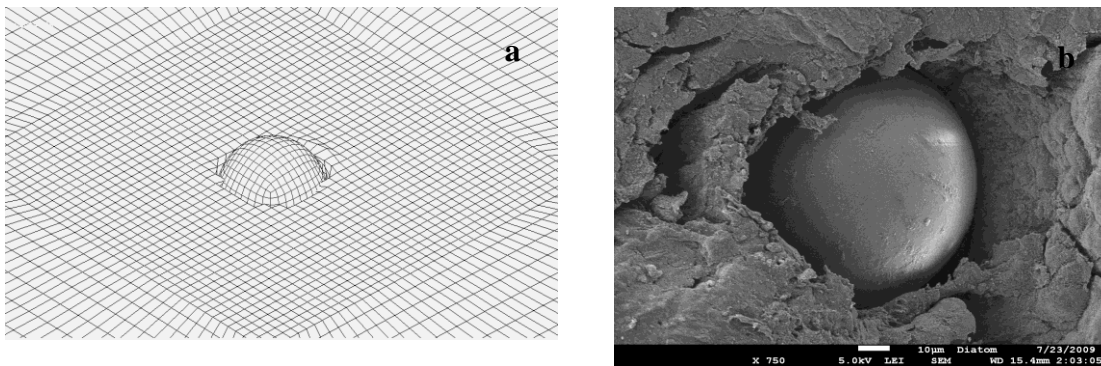


Figure 5-8 Eroder capture at perpendicular impact (a) simulation (b) experiments



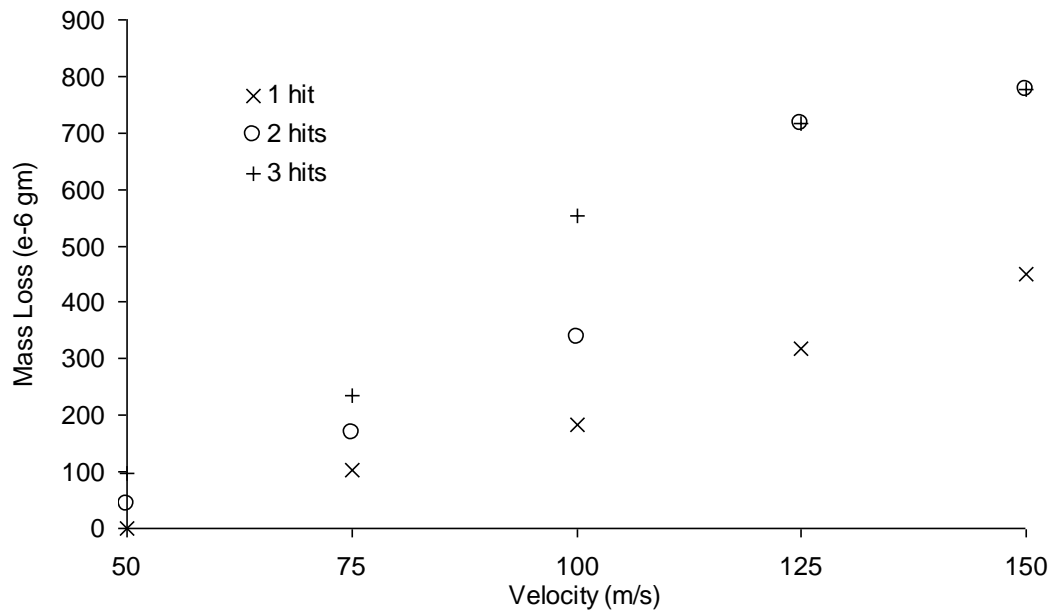


Figure 5-9 Mass loss vs. impact velocity for perpendicular impact and d/s 0.1. Critical stress for material failure was 12.5 MPa; plot compares the erosion magnitude for successive impacts at fixed angularity of 0.1

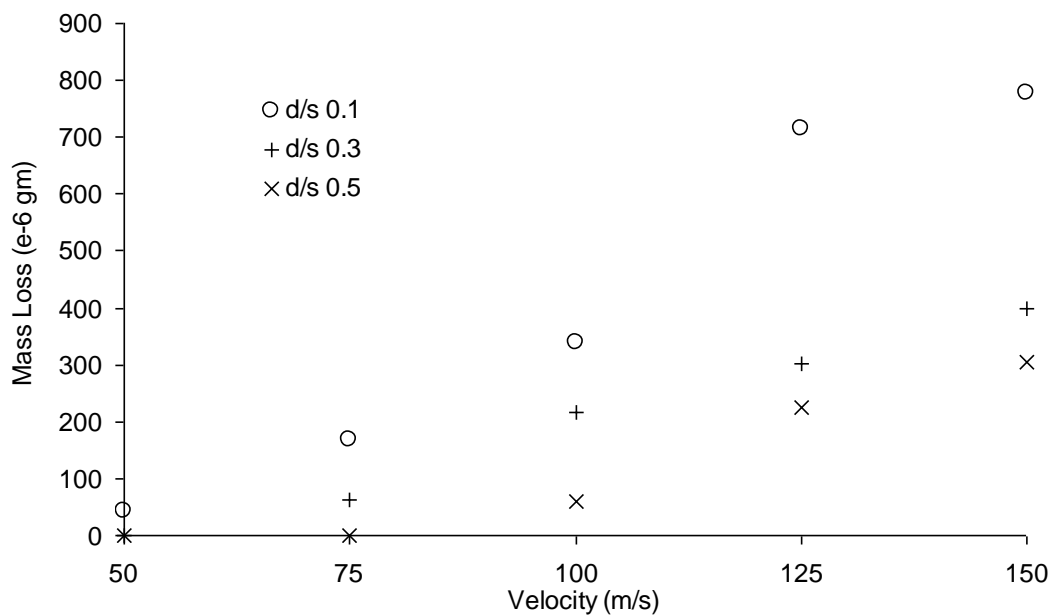


Figure 5-10 Mass loss vs. impact velocity after 2 perpendicular impacts. Critical stress for material failure was 12.5 MPa; plot compares the erosion magnitude after 2 impacts by erodents of different angularity

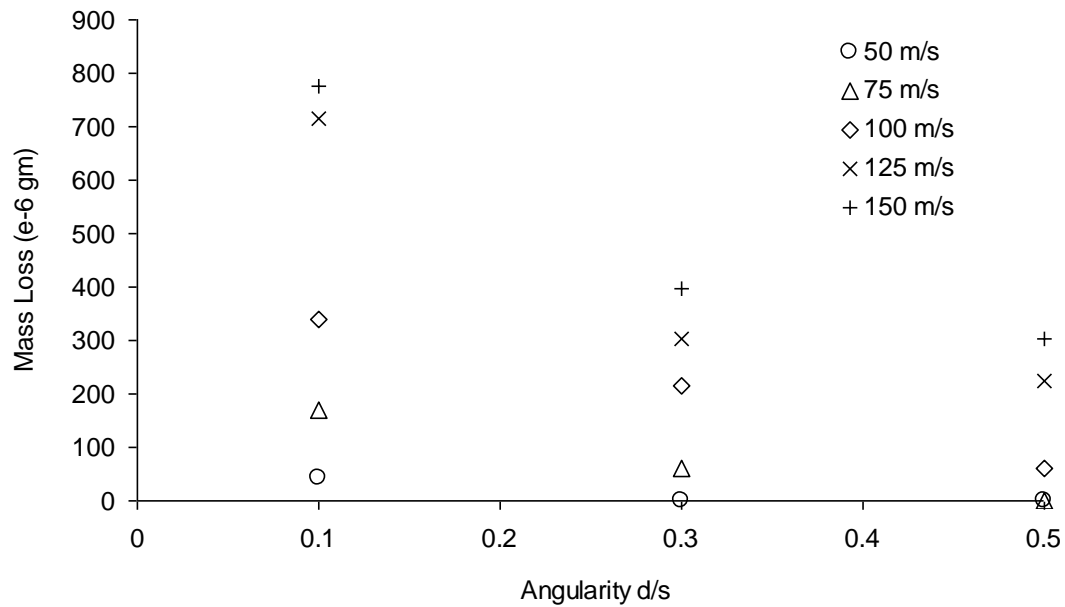


Figure 5-11 Mass loss vs. angularity after 2 perpendicular impacts.  
Critical stress for material failure= 12.5 MPa; plot compares the erosion at different impact velocities

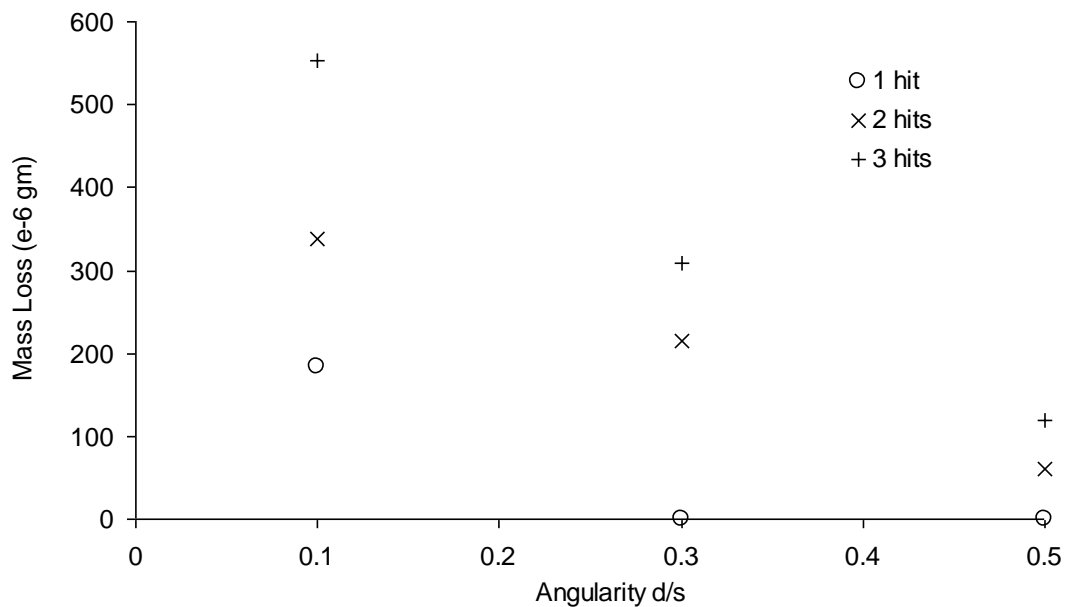


Figure 5-12 Mass loss vs. angularity at 100 m/s impact velocity.  
Critical stress for material failure= 12.5 MPa; plot compares the erosion after successive impacts at 100 m/s

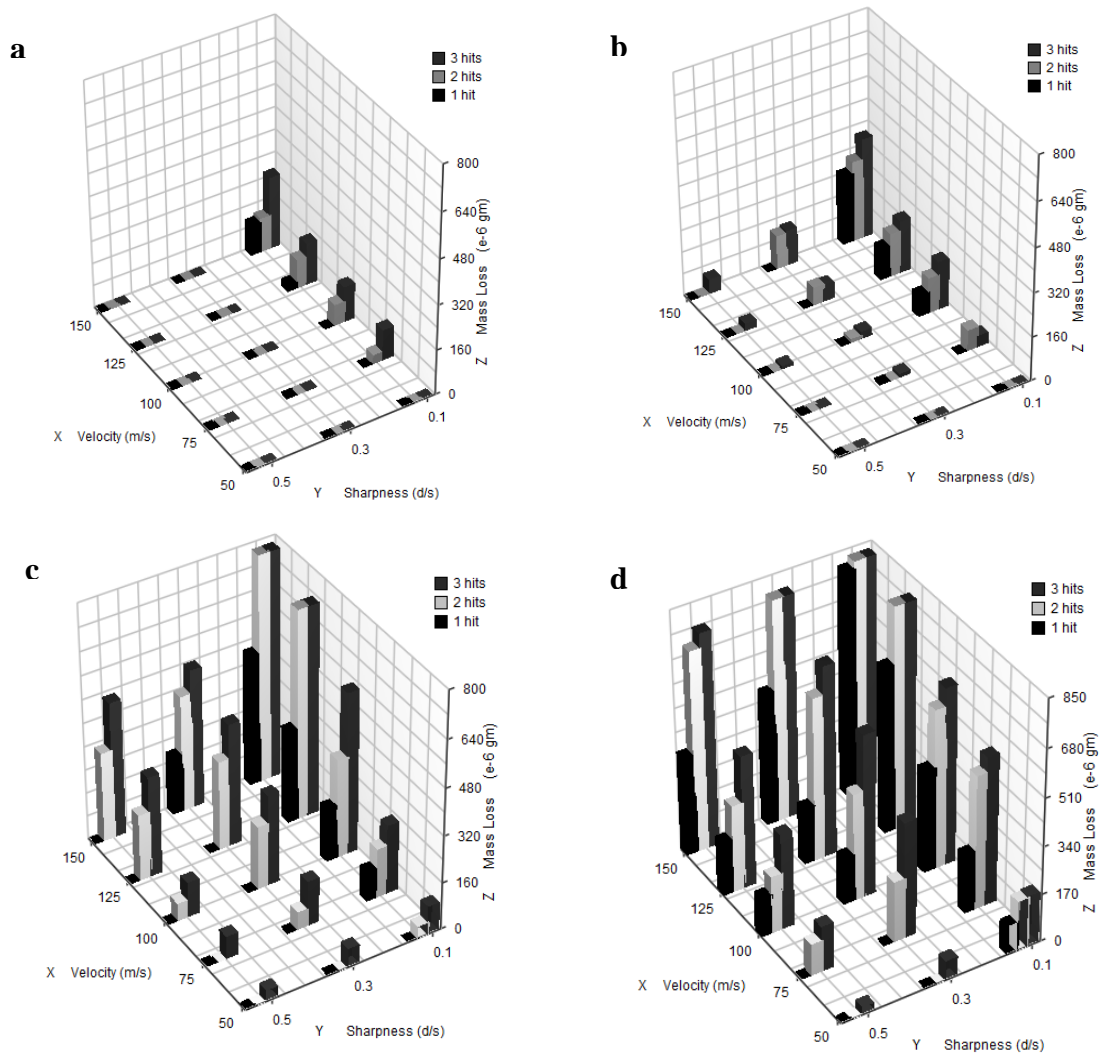


Figure 5-13 Histograms of erosion mass loss for different critical stresses.

(a) 13.5 MPa (b) 13 MPa (c) 12.5 MPa (d) 12 MPa

Histograms compare erosion at different velocities and angularities for successive impacts

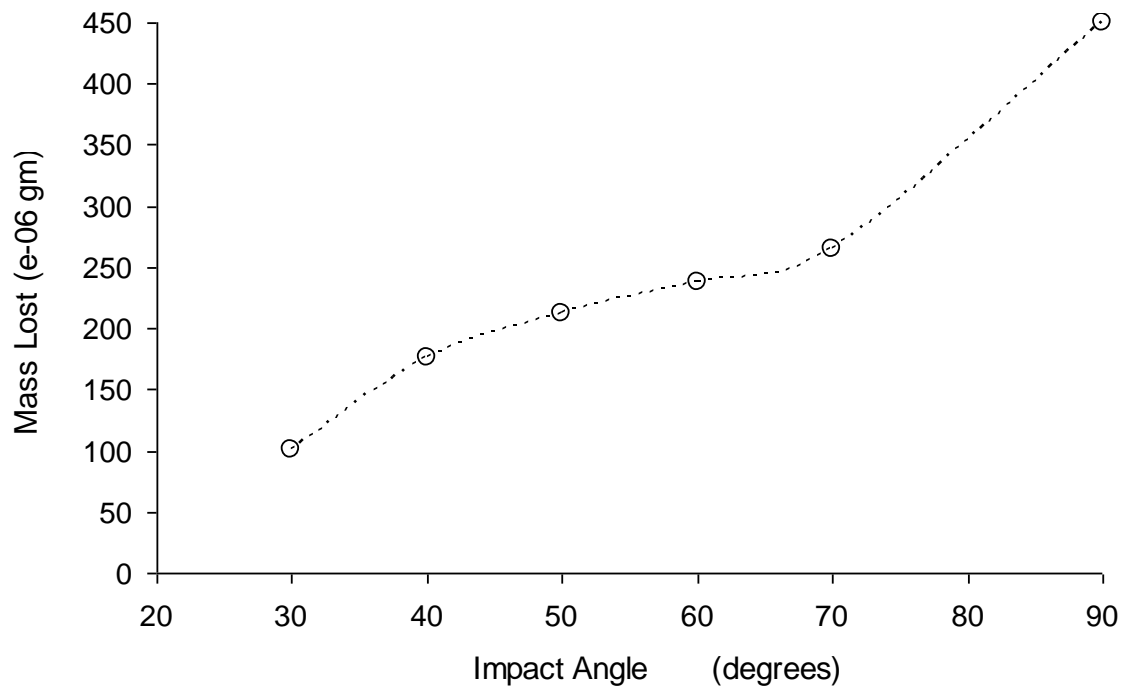


Figure 5-14 Mass loss vs. impact angle.  
Single impact at 150 m/s with erodent of d/s 0.1

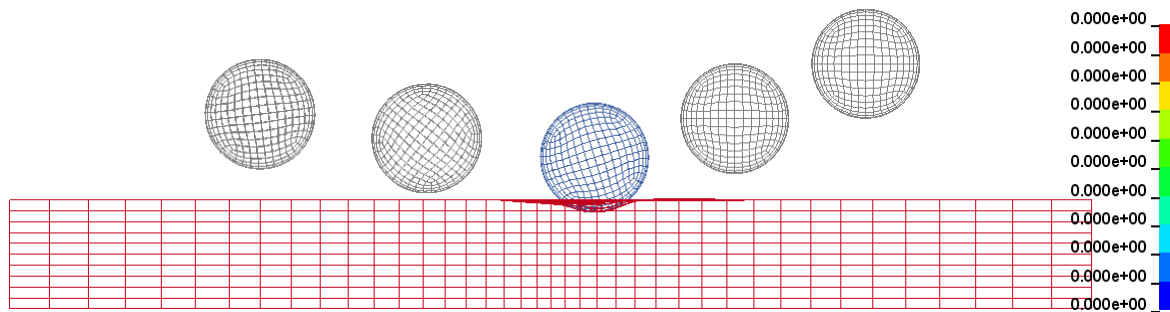


Figure 5-15 Inclined impact by a spherical erodent, d/s 0.1, 150 m/s.  
Side view, showing absence of contours of plastic strain under impact zone for 30 degree impact.  
Impingement was from right to left. The colored erodent corresponds to the time-state when the snapshot was taken, whereas the grayscale erodents represent the trajectory of the erodent before and after the impact.

### 5.2.2. IMPACT WITH SHARP ERODENT

The details of the FE mesh used in these simulations are (according to conventions specified in Section 3.2.2):

$$s = 3.16 \text{ mm}$$

$$s' = 2 \text{ mm}$$

$$h = 1 \text{ mm}$$

$$e_b = 0.05 \text{ mm}$$

$$V = 50 \text{ m/s}$$

$$\alpha = 20^\circ, 30^\circ, 40^\circ, 50^\circ, 60^\circ \text{ and } 90^\circ$$

The mesh geometry of the target has been reduced in size to reduce the computation and storage costs. Inclined impact simulations were performed with the sharp erodent (Figure 3-4) at incidence angles of  $20^\circ$ ,  $30^\circ$ ,  $40^\circ$ ,  $50^\circ$ ,  $60^\circ$  and  $90^\circ$ .

Figure 5-16 shows the topography of the eroded mesh at perpendicular impact and  $30^\circ$  impact. It is obvious from this figure that the amount of material removed is higher in the case of inclined impact. Figure 5-17 shows the iso-surfaces of contours of effective stress in the PUR target for the perpendicular and inclined impacts, whereas Figure 5-18 shows the iso-surfaces of contours of plastic strain for. When the quantities of mass loss is plotted against the impact angle the erosion curve as shown in Figure 5-19 is obtained which clearly displays a maxima at  $30^\circ$ . This result is in agreement to the trends noticed in literature (Figure 2-13 and Figure 2-10) and resolves the apparent disparity exhibited by the trend in Figure 5-14. The reason behind the successful capturing of the mass-loss maxima by the sharp erodent can be explained by recognizing the processes undergoing during the glancing impact as shown in Figure 5-17 and Figure 5-18. The fracture

criterion was excluded for these simulations to enable accumulation of residual deformation. Clearly the perpendicular impact causes higher stress levels, Figure 5-17 (a), than the inclined impact (though the maximum stress attained in inclined impact is higher than the specified critical stress of 12.5 MPa). However, Figure 5-18 (b) shows that for the inclined case, the lateral inertia (due to the horizontal velocity component) causes the sharp tip to be dragged along a longer distance on the surface of the target thereby causing a larger deformation zone than that formed during perpendicular impact. This implies that when the fracture is incorporated in the simulation, material will be removed all over that larger deformed zone; it doesn't matter if locally the stress levels are higher for the perpendicular impact because fracture would still occur only at the specified threshold. Thus, the sharp erodent captures the mass-loss maxima at low angles by virtue of its 'ploughing' action, i.e. subjecting a larger area of the target surface to the detrimental effects of the cutting tip.

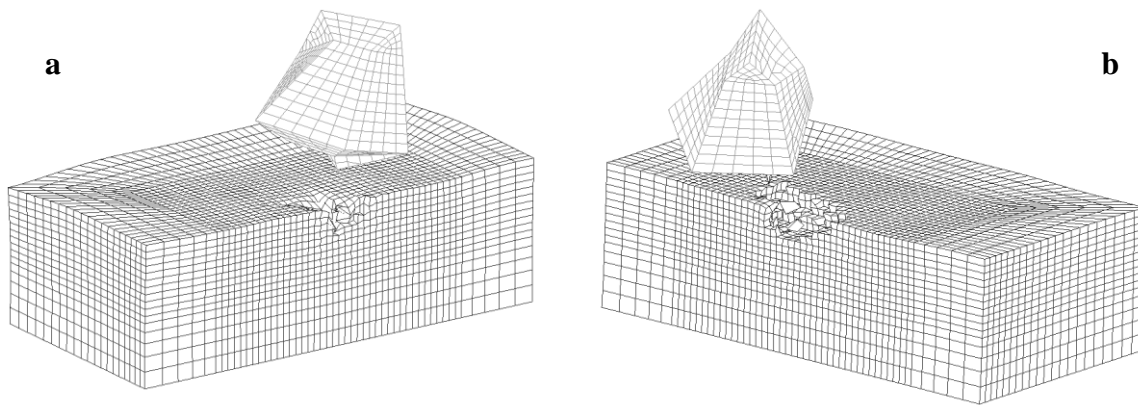


Figure 5-16 Topography of eroded mesh after impact by sharp erodent.  
Incidence angle (a) 90°, (b) 30°. One half of the target mesh has been masked for clarity. Erodent trajectory for the 30° impact was from right to left

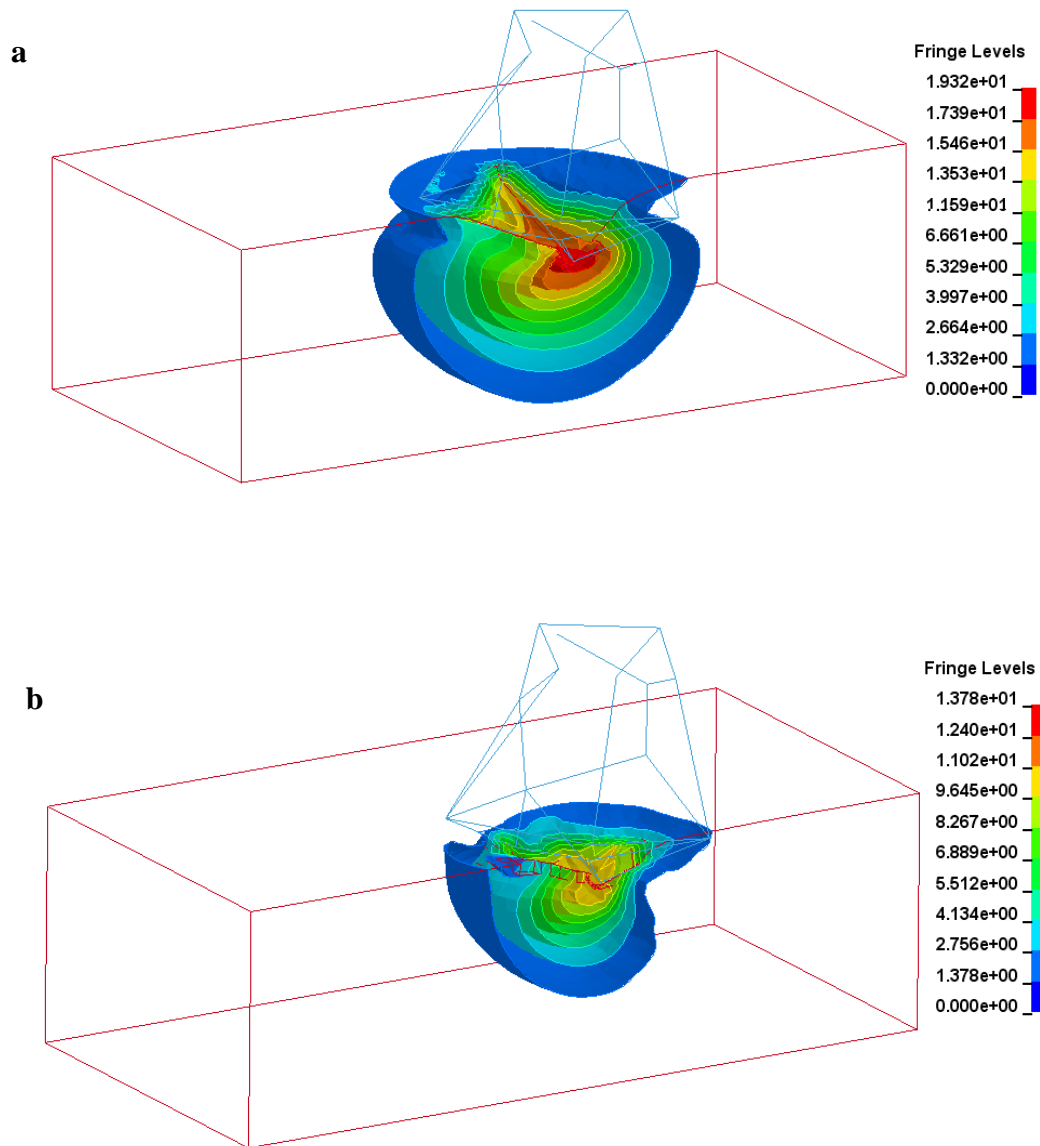


Figure 5-17 Isosurfaces of contours of effective stress in the PUR target.  
Incidence angle (a) 90°, (b) 30°. One half of the target mesh has been masked for clarity. Eroder trajectory for the 30° impact was from right to left

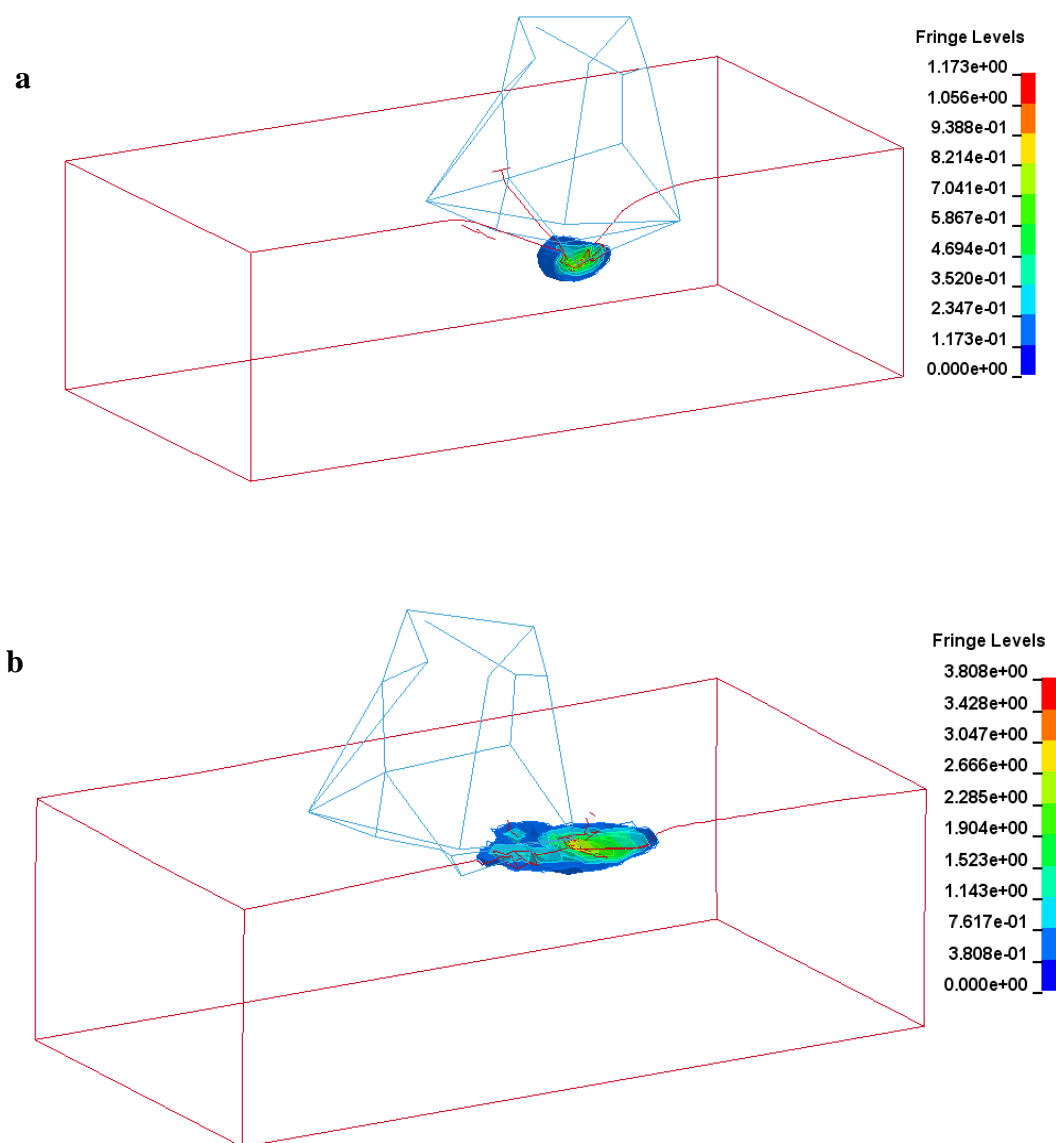


Figure 5-18 Isosurfaces of contours of plastic strain on deformed zone.  
 Incidence angle (a) 90°, (b) 30°. One half of the target mesh has  
 been masked for clarity. Eroder trajectory for the 30° impact was from right to left



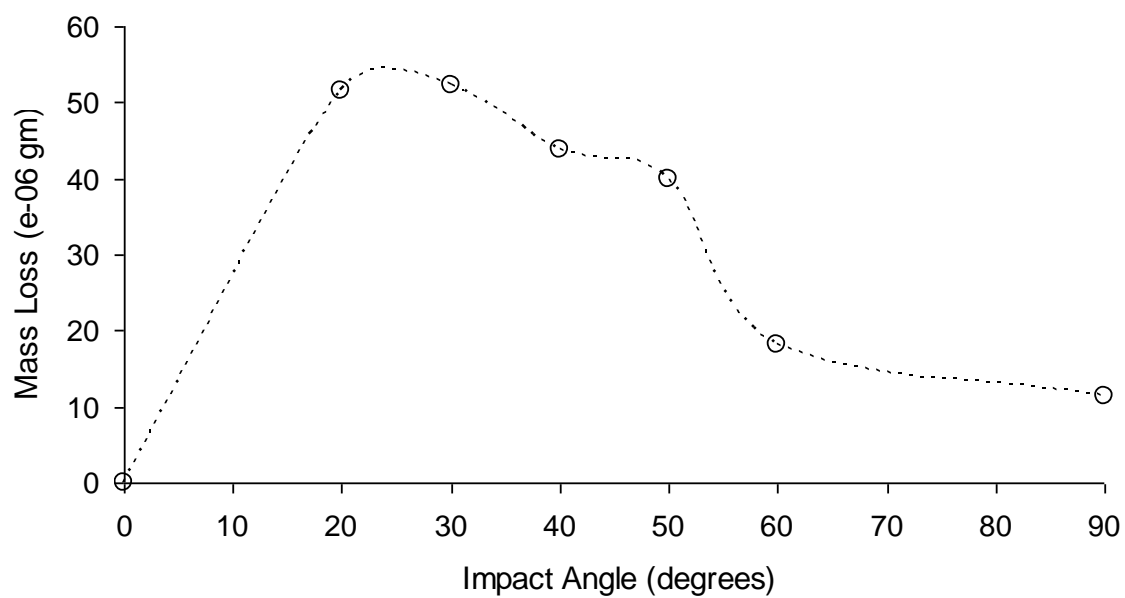


Figure 5-19 Mass loss vs. impact angle erosion curve for sharp erodent.  
Velocity of impact = 50 m/s. Plot shows the distinct maxima at low impact angles.

## 6. SUMMARY AND CONCLUSION

A comprehensive study has been performed on erosion simulation of polyurethane films subjected to impact by sand particles. The polyurethane film has been modeled as a block on a substrate and the erodents as either spherical or discretely sharp particles. Bi-directional periodic boundary conditions have been invoked in the simulations and a novel descriptor for angularity,  $\bar{\beta}$ , has been defined as the corner radius of an erodent normalized over the spacing of the erodent distribution. An elasto-plastic material constitution with an effective stress to failure type fracture criterion has been utilized to model the deformation and fracture characteristics of polyurethane. In the first set of finite element calculations, the fracture criteria has been suppressed to study only the deformation characteristics of polyurethane under perpendicular impact by erodents of varying angularity defined by  $\bar{\beta}$ . By approximating the impact crater as an inverted spherical cap the volume of the deformed zone has been quantified and plotted against the angularity parameter to yield the first result in known literature that reveals the deleterious effect of erodent angularity on erosion severity. Following this, the endeavor has been extended to erosion quantification by adding the fracture criteria in the simulation framework which enabled measurement of the mass lost due to erosion. For perpendicular impact, the erosion curves of mass loss as a function of velocity and number of co-incident impacts show good correlation with the trends seen in literature and the curves for mass loss vs. angularity concurred with the qualitative estimates obtained from the initial deformation analysis. The erosion curve for inclined impact with spherical erodents, however, failed to capture the maxima at lower angles as seen in literature, because the limited numbers of hits performed in the simulations were not

sufficient to breach the threshold in inclined impact and cause erosion. It is anticipated that with a multitude of impact, fatigue mechanisms would set in, and the low-angle maxima of the erosion curve can be captured even with the spherical erodent. However, to accelerate the process, a workable solution was found by using a discretely modeled erodent with faceted surfaces and sharp cutting edges which lead to locally high stresses at the point of impact. In an inclined impact simulation, this cutting point was dragged by the lateral inertia thereby affecting a larger zone than in perpendicular impact, thus showing a peak of the erosion curve at around  $30^\circ$  which is in agreement with data in literature.

Future work will focus on improving the predictability of the simulation framework. To achieve this, two activities have to progress in parallel. Firstly, to fully capture the macroscopic mechanical response of polyurethane, a more enriched material constitution with rate, temperature and pressure sensitivity and a pressure driven failure criteria to account for the triaxialities of impact has to be incorporated in the simulation. This would also require extensive mechanical and fracture tests, in a controlled manner, on bulk polyurethane, to estimate the myriad of material parameters that characterize such enriched material models. Secondly, the solid particle impact scenario has to be modeled in a manner that resembles, more closely, the phenomena of erosion. This can be achieved by addressing currently unaddressed (in simulation) erosion variables like erodent rotation, flux etc. and desirably with unlimited computational resources, by simulating stochastic impacts by millions of particles as in reality. Addressing these issues will improve the predictive capability of the simulation framework and lead to better understanding of the mechanisms underlying solid particle erosion.

## REFERENCES

1. J. G. A. Bitter, A study of erosion phenomena Part-I, *Wear* 6 (1963) 5-21.
2. I. Finnie, Erosion of surfaces by solid particles, *Wear* 3 (1960) 87-103.
3. G. P. Tilly, Erosion caused by airborne particles, *Wear* 14 (1969) 63-79.
4. D. Aquaro, E. Fontani, Erosion of ductile and brittle materials, *Meccanica* 36 (2001) 651-661.
5. G. P. Tilly, A two stage mechanism of ductile erosion, *Wear* 23 (1973) 87-96.
6. J. G. A. Bitter, A study of erosion phenomena Part-II, *Wear* 6 (1963) 169-190.
7. I. M. Hutchings, J. C. Arnold, The mechanisms of erosion of unfilled elastomers by solid particle impact, *Wear* 138 (1990) 33-46.
8. I. M. Hutchings, J. C. Arnold, A model for the erosive wear of rubber at oblique impact angles, *J Phys D: Appl Phys* 25 (1992) A222-A229.
9. I. M. Hutchings, R. E. Winter, Solid particle erosion studies using single angular particles, *Wear* 29 (1974) 181-194.
10. S. Bahadur, R. Badruddin, Erodent particle characterization and the effect of particle size and shape on erosion, *Wear* 138 (1990) 189-208.
11. M. A. Verspui, P. van der Velden, G. de With, P. J. Slikkerveer, Angularity determination of abrasive powders, *Wear* 199 (1996) 122-126.
12. G. W. Stachowiak, Particle angularity and its relationship to abrasive and erosive wear, *Wear* 241 (2000) 214-219.
13. H. C. Meng, K. C. Ludema, Wear models and predictive equations: their form and content, *Wear* 181-183 (1995) 443-457.

14. I. M. Hutchings, J. C. Arnold, Erosive wear of rubber by solid particles at normal incidence, *Wear* 161 (1993) 213-221.
15. Q. Chen, D. Y. Li, Computer simulation of solid particle erosion of composite materials, *Wear* 225 (2003) 78-84.
16. D. Y. Li, E. Khaled, M. J. Anderson, S. Chiovelli, A microscale dynamical model for wear simulation, *Wear* 225-229 (1999) 380-386.
17. K. Shimizu, T. Noguchi, FEM analysis of erosive wear, *Wear* 250 (2001) 779-784.
18. D. Griffin, A. Daadbin, S. Datta, The development of a three-dimensional finite element model for solid particle erosion on an alumina scale/MA956 substrate, *Wear* 256 (2004) 900-906.
19. M. S. ElTobgy, M. A. ElBestawi, E. Ng, Finite Element Modeling of erosive wear, *International Journal of Machine Tools and Manufacturing* 45 (2005) 1337-1346.
20. P. J. Woytowicz, R. H. Richman, Modeling of damage from multiple impacts by spherical particles, *Wear* 233-235 (1999) 120-133.
21. Y. F. Wang, Z. G. Yang, Finite element model of erosive wear on ductile and brittle materials, *Wear* 233-235 (2008) 120-133.
22. J. F. Molinari, M. Ortiz, A study of solid-particle erosion of metallic targets, *International Journal of Impact Engineering* 27 (2002) 347-358.
23. I. M. Hutchings, R. E. Winter, J. E. Field, Solid particle erosion of metals: the removal of surface material by spherical projectiles, *Proc R Soc London* 348 (Ser A) (1976) 379-392.

24. M. Takaffoli, M. Papini, Finite element analysis of single impacts of angular particles on ductile targets, *Wear* 267 (2009) 144-151.
25. B. Zouari, M. Touratier, Simulation of organic coating removal by particle impact, *Wear* 253 (2002) 488-497.
26. G. J. Dvorak, Y. A. Bahei-El-Din, Enhancement of blast resistance of sandwich plates, *Composites Part B: Engineering* 39 (1) (2008) 120-127.
27. Z. Xue, J. W. Hutchinson, Neck retardation and enhanced energy absorption in metal-elastomer bilayers, *Mechanics of Materials* 39 (2007) 473-487.
28. M. R. Amini, J. Simon, S. Nemat-Nasser, Numerical modeling of effect of polyurea on response of steel plates to impulsive loads in direct pressure-pulse experiments, *Mechanics of Materials* 42 (2010) 615-627.
29. A. V. Amirkhizi, J. Isaacs, J. McGee, S. Nemat-Nasser, An experimentally-based viscoelastic constitutive model for polyurea, including pressure and temperature effects, *Philosophical Magazine* 86 (36) (2006) 5847-5866.
30. P. A. Du Bois, D. J. Benson, S. Kolling, W. W. Feng, A tabulated formulation of hyperelasticity with rate effects and damage, *Comput Mech* 40 (2007) 885-899.
31. P. A. Du Bois, D. J. Benson, S. Kolling, A simplified approach for strain-rate dependent hyperelastic materials with damage, 9th International LS-Dyna Users Conference, (2006) Dearborn, MI, USA.
32. J. S. Bergstrom, M. C. Boyce, Constitutive modeling of the large strain time-dependent behavior of elastomers, *J. Mech Phys Solids* 46 (5) (1998) 931-954.
33. K. A. Chowdhury, A. A. Benzerga, R. Talreja, A computational framework for analyzing the dynamic response of glassy polymers, *Computer Methods in Applied Mechanics and Engineering* 197 (49-50) (2008) 4485-4502.

34. T. Deng, M. S. Bingley, M. S. A. Bradley, The influence of particle rotation on the solid particle erosion rate of metals, *Wear* 256 (2004) 1037-1049.
35. I. Finnie, Some reflections on the past and future of erosion, *Wear* 186-187 (1995) 1-10.
36. T. Belytschko, L. P. Bindeman, Assumed strain stabilization of eight node hexahedral element, *Comp Meth Appl Mech Eng* 105 (1993) 225-260.
37. J. O. Hallquist, *LS-Dyna Theory Manual*, Livermore Software Technology Corporation, 2006.
38. R. D. Krieg, S. W. Key, Implementation of a time dependant plasticity theory into structural computer programs, *Constitutive equations in viscoplasticity: Computational and Engineering Aspects* 20 (125-137) (1976)
39. E. Tocha, H. Janik, M. Debowski, G. J. Vancso, Morphology of polyurethanes revisited by complementary AFM and TEM, *Journal of Macromolecular Science Part B- Physics* B41 (4-6) (2002) 1291-1304.
40. E. M. Arruda, M. C. Boyce A three-dimensional constitutive model for the large stretch behavior of rubber elastic materials, *Journal of the Mechanics and Physics of Solids* 41 (2) (1993) 389-412.
41. D. Peirce, C. F. Shih, A. Needleman, A tangent modulus method for rate dependent solids, *Computers & Structures* 18 (5) (1984) 875-887.
42. K. A. Chowdhury, R. Talreja, A. A. Benzerga, Effects of Manufacturing-Induced Voids on Local Failure in Polymer-Based Composites, *J Eng Mater Technol* 130 (2) (2008) 021010 1 - 021010 9.

## APPENDIX A

The broader perspective of polymer-film erosion in mind, a preliminary study, with an enriched rheological material model, was conducted by performing low to medium velocity impact analysis on films of polymeric material (with known parameters e.g. PMMA, PS) thereby allowing an estimation of the deformation behavior and probable failure mechanisms of such polymeric films under dynamic loading and also a validation of the advanced Macromolecular constitution of the code in use. In the following sections the details of the baseline study i.e. the geometry of the model, the finite element mesh and associated boundary conditions, the finite element formulation, material model and material parameters etc. is presented by along with results and associated discussions.

### Geometry:

The polymeric coating is modeled as a 50mm x10mm planar polymeric block, without the substrate, and discretized as a plane strain problem, with displacement boundary conditions along the entirety of one edge of the block and velocity boundary conditions imposed on those nodes of the other edge where a striker (width 5.5mm) is simulated to impact the block as shown in Fig.A1.

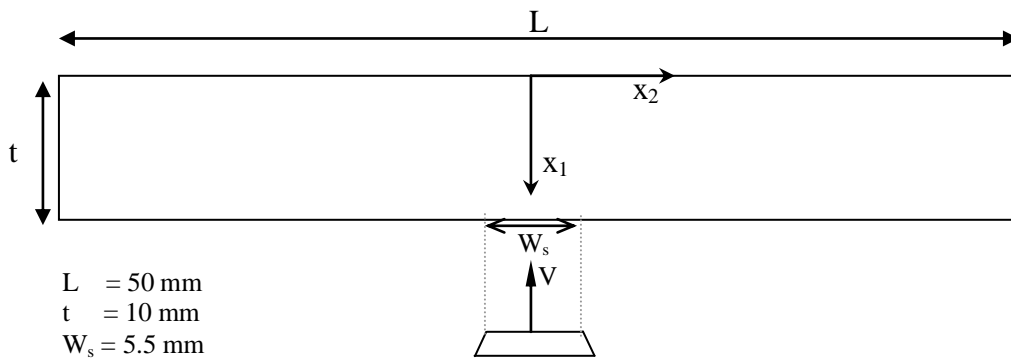


Figure A1. Problem Geometry (not to scale)



Finite element mesh:

Because of symmetry of the specimen about the  $x_1$  axis only one-half of the same is considered for simulation. The finite element mesh as shown in Fig.A2 consists of a total of 775 ( $25 \times 31$ ) quadrilateral elements and 832 nodes. The mesh density is biased towards the impact location i.e. in  $x_2$  direction there are more number of elements where the striker impacts the specimen and vice-versa in the  $x_1$  direction. Such type of biasing has a twofold advantage of having a low element aspect-ratio (i.e. higher width) near the impact point and also in decreasing the total number of elements in the mesh thus the reducing the computation time. An equivalent uniform mesh of the same specimen would have 1250 elements and 1326 nodes.

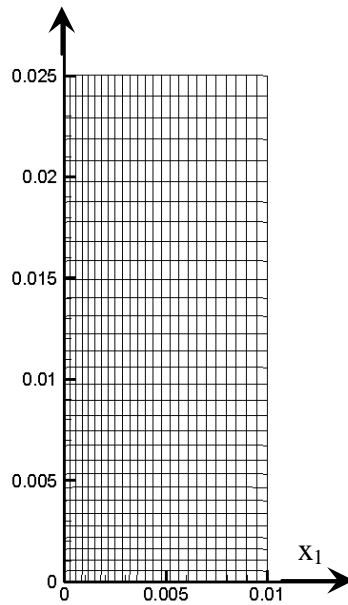


Figure A2. Specimen Mesh (units in meter, not to scale)

Boundary Conditions:

The constrained edge and the impacting striker are accounted for by prescribing the following boundary conditions:

$$\mathbf{u}_1 = \mathbf{0} \quad \text{for } \mathbf{x}_1 = \mathbf{0} \text{ and } |\mathbf{x}_2| \leq L/2; \quad (\text{A.1})$$

$$\mathbf{u}_2 = \mathbf{0} \quad \text{for } |\mathbf{x}_1| \leq t \text{ and } \mathbf{x}_2 = \mathbf{0} \quad (\text{A.2})$$

$$\dot{\mathbf{u}}_2 = -\mathbf{V}_2(t) \text{ for } \mathbf{x}_1 = t \text{ and } |\mathbf{x}_2| \leq W_s/2 \quad (\text{A.3})$$

Finite Element Formulation:

This section discusses the nuances of FEA and the advanced material constitution that were employed in this endeavor. The in-house impact code used for this project performs full transient analysis using a Lagrangian formulation of the field equations following the methodology of Chowdhury et al. [33]. The material constitution follows the modified Macromolecular model which accounts for pressure, rate and temperature sensitivity along with an orientation hardening characteristic of polymer networks.

Field Equations and Numerical Methods:

The dynamic principle of virtual work is written as

$$\int_V \boldsymbol{\tau}^{ij} \delta \eta_{ij} dV = \int_S T^i \delta u_i dS - \int_V \rho \frac{\partial^2 u^i}{\partial t^2} \delta u^i dV \quad (\text{A.4})$$

where

$\boldsymbol{\tau}^{ij} = J \boldsymbol{\sigma}^{ij}$ , are the contravariant components of Kirchoff stress

$\boldsymbol{\sigma}^{ij}$  are the components of Cauchy Stress

$J = \sqrt{\det(\mathbf{g}_{ij}) / \det(\mathbf{G}_{ij})}$ , is the ratio of current to reference volume

$\mathbf{g}_{ij}$  and  $\mathbf{G}_{ij}$  are the inverse of metric tensors in current and reference configurations

$\mathbf{T}^i = (\boldsymbol{\tau}^{ij} + \boldsymbol{\tau}^{kj} \mathbf{u}^i_{,k}) \mathbf{v}_j$ , are the contravariant surface tractions

$\eta_{ij} = (u_{i,j} + u_{j,i} + u^k_{,i} u_{k,j})$ , are the covariant components of Green-Lagrange strain

$u^i$  are the covariant displacements,

$\rho$ ,  $V$  and  $S$  are the mass density, volume and surface area of the body in reference configuration respectively.

The FEA implementation of the problem is based on discretization using linear displacement triangular elements arranged in quadrilaterals of ‘four crossed’ elements and an assumption of plane strain. The equations of motion obtained from substituting the FE discretization into (A.4) are of the form

$$\mathbf{M} \frac{\partial^2 \mathbf{U}}{\partial t^2} = \mathbf{F} \quad (\text{A.5})$$

where  $\mathbf{M}$  is a lumped mass matrix,  $\mathbf{U}$  are the nodal displacements and  $\mathbf{F}$  the nodal forces.

Integration of the equations of motion (A.5) using the Newmark- $\beta$  method delivers the updated global velocities and displacements following which the deformation gradient, strain rate and other kinematic quantities are directly calculated.

Material Constitution:

The rate of deformation is decomposed into an elastic part  $\mathbf{D}^e$  and a visco-plastic part  $\mathbf{D}^p$ .

$$\mathbf{D} = \mathbf{D}^e + \mathbf{D}^p \quad (\text{A.6})$$

Elastic part of the response is expressed by a Hypoelastic law in terms of Jaumann

derivative  $[\overset{\nabla}{\boldsymbol{\sigma}} = \dot{\boldsymbol{\sigma}} - \mathbf{W}\boldsymbol{\sigma} + \boldsymbol{\sigma}\mathbf{W}]$  of Cauchy stress tensor,

$$\overset{\nabla}{\boldsymbol{\sigma}} = \mathbf{L} : \mathbf{D}^e \quad (\text{A.7})$$

where  $\mathbf{L}$  is the isotropic tensor (4<sup>th</sup> order) of elastic moduli and thus depends on material constitution. The viscoplastic part  $\mathbf{D}^p$  is expressed by a non-associative flow rule which is rate-sensitive and treats the plastic deformation as incompressible.

$$\mathbf{D}\mathbf{p} = \dot{\varepsilon} \frac{3}{2} \frac{\boldsymbol{\sigma}'_d}{\sigma_{eq}} \quad (\text{A.8})$$

where  $\mathbf{p} = \frac{3}{2} \frac{\boldsymbol{\sigma}'_d}{\sigma_{eq}}$ , is the direction of plastic flow and  $\sigma_{eq}$  is effective stress, defined as

$$\sigma_{eq} = \sqrt{\frac{3}{2} \boldsymbol{\sigma}'_d : \boldsymbol{\sigma}'_d} \quad (\text{A.9})$$

and  $\boldsymbol{\sigma}'_d$  is the deviatoric part of the driving stress  $\boldsymbol{\sigma}_d$ , given by

$$\boldsymbol{\sigma}_d = \boldsymbol{\sigma} - \mathbf{b} \quad (\text{A.10})$$

where  $\boldsymbol{\sigma}$  is the Cauchy stress tensor and  $\mathbf{b}$  is the back stress tensor which describes the orientation hardening of the material.

$$\dot{\mathbf{b}} = \mathbf{R} : \mathbf{D} \quad (\text{A.11})$$

where  $\mathbf{R}$  is the back-stress moduli, specified by using a non-Gaussian network model combining classical 3-chain and 8-chain models,

$$\mathbf{R} = (\mathbf{1} - \kappa) \mathbf{R}_{3\text{-ch}} + \kappa \mathbf{R}_{8\text{-ch}} \quad (\text{A.12})$$

$$\kappa = 0.85 \bar{\lambda} / \sqrt{N} \quad (\text{A.13})$$

where  $\bar{\lambda}$  is the maximum principal stretch and  $N$  is a material constant.

Strain rate effects are incorporated using the Boyce et al. [40] modified formulation which accounts for pressure, temperature sensitivity and strain-softening effects. Thus the effective viscoplastic strain rate is given by

$$\dot{\varepsilon} = \dot{\varepsilon}(\sigma_{eq}) = \dot{\varepsilon}_0 \exp \left[ -\frac{A(s - \alpha \sigma_{kk})}{T} \left( 1 - \left( \frac{\sigma_{eq}}{s - \alpha \sigma_{kk}} \right)^{5/6} \right) \right] \quad (\text{A.14})$$

where  $\sigma_{kk}$  is the trace of the hydrostatic stress;

$\dot{\epsilon}_0$ ,  $\mathbf{A}$  and  $\alpha$  parameters that independently affect the rate, temperature and pressure sensitivity of the material respectively;  $\mathbf{s}$  is the microscale athermal shear strength whose evolution is governed by

$$\dot{\mathbf{s}} = h_1 \left( 1 - \frac{\mathbf{s}}{\mathbf{s}_1} \right) \dot{\bar{\epsilon}} + h_2 \left( 1 - \frac{\mathbf{s}}{\mathbf{s}_2} \right) \dot{\bar{\epsilon}} \quad (\text{A.15})$$

where  $\mathbf{h}$  is the slope of the yield drop with respect to plastic strain and  $\mathbf{s}_0$  and  $\mathbf{s}_{1,2}$  are the initial and saturation values of  $\mathbf{s}$  respectively.

The constitutive updating is based on integrating the incremental effective strain according to the rate-tangent method [41] which per se improves the numerical stability.

Thus modification of (A.7) as

$$\overset{\nabla}{\boldsymbol{\sigma}} = \mathbf{L} : \mathbf{D}^e = \mathbf{L} : (\mathbf{D} - \mathbf{D}^{vp}) = \mathbf{L} : \mathbf{D} - \mathbf{L} : \mathbf{p} \dot{\bar{\epsilon}} = \mathbf{L} : \mathbf{D} - \mathbf{P} \dot{\bar{\epsilon}} \quad (\text{A.16})$$

where, incremental effective strain is given by

$$\dot{\bar{\epsilon}} = \left[ (1 - \theta) \dot{\bar{\epsilon}}_t + \theta \dot{\bar{\epsilon}}_{t+\Delta t} \right] \quad (\text{A.17})$$

leading to

$$\overset{\nabla}{\boldsymbol{\sigma}} = \mathbf{L}^{\text{tan}} : \mathbf{D} - \frac{\dot{\bar{\epsilon}}_t}{1 + \xi} \mathbf{P} \quad (\text{A.18})$$

where

$$\mathbf{L}^{\text{tan}} = \mathbf{L}^e - \frac{\xi}{(1 + \xi)} \frac{\mathbf{P} \mathbf{P}}{H} \quad (\text{A.19})$$

$$\mathbf{P} = G \frac{3 \boldsymbol{\sigma}'_d}{\sigma_{eq}} \quad (\text{A.20})$$

$$\xi = \theta \Delta t \frac{\partial \dot{\bar{\epsilon}}}{\partial \sigma_{eq}} H \quad (\text{A.21})$$

$$H = \left( 3G + \frac{9}{4\sigma_{eq}^2} \boldsymbol{\sigma}'_d \cdot \mathbf{R}' \boldsymbol{\sigma}'_d \right) \quad (\text{A.22})$$

and  $\mathbf{R}'$  is a deviator of deviator of the back-stress moduli defined through (A.11) and (A.12).

### Material Parameters:

The two materials used in this endeavor are Polystyrene (PS) and Poly-methyl Methacrylate (PMMA).

The material parameters representative of Polystyrene were taken from [33] with  $\rho = 1300 \text{ kg/m}^3$ ,  $E = 735 \text{ MPa}$ ,  $\nu = 0.3$ ,  $s_0 = 97 \text{ MPa}$ ,  $s_{1,2} = 46 \text{ and } 103 \text{ MPa}$ ,  $A = 296 \text{ K/MPa}$ ,  $h = 81 \text{ MPa}$ ,  $\alpha = 0.08$ ,  $N = 7$  and  $C_R = 7.25 \text{ MPa}$ .

The parameters corresponding to PMMA were  $\rho = 1100 \text{ kg/m}^3$ ,  $E = 3.2 \text{ GPa}$ ,  $\nu = 0.33$ ,  $s_0 = 70 \text{ MPa}$ ,  $s_{1,2} = 114 \text{ and } 103 \text{ MPa}$ ,  $A = 225 \text{ K/MPa}$ ,  $h = 1300 \text{ MPa}$ ,  $C_R = 9.5 \text{ MPa}$ ,  $\alpha = 0.02$ ,  $N = 5.1$ ,  $C_R = 7.25 \text{ MPa}$ ; these were taken from [42]. The only slight modifications were in the values of the reference strain rate  $\dot{\epsilon}_0$  which took the values of  $2 \times 10^{19} \text{ s}^{-1}$  and  $2 \times 10^{21} \text{ s}^{-1}$  for PMMA and PS respectively to account for the extent of higher nominal strains (order of  $10^3$ ) being experienced.

### Analysis:

Impact analyses (under plane strain assumption in the  $x_1$ - $x_2$  plane) were carried out on the polymeric block. All simulations were performed at room temperature (i.e.  $T_0 = 298 \text{ K}$ ) for a set of five impact velocities ( $V_1$ ) 10m/s to 50m/s with increments of 10m/s. The velocity function  $V(t)$  was a ramp with a rise time  $t_r$  of  $2\mu\text{s}$  and final constant velocity of  $V_1$ . Also,  $\theta = 0.55$  was used in the rate-tangent numerical time integration scheme. No failure criteria (viz. crazing) were incorporated in this set of analyses in order to focus solely on the deformation behavior of the polymer in impact loading,

## Results:

The impact analysis results are presented in this section in the form of contour plots of the accumulated plastic strain and the maximum principal stress followed by the Load-Displacement curves and curves of Maximum Principal Stress plotted against displacement at various velocities for the materials PMMA and PS.

Typical load vs. displacement curves are shown in Figure A.5. A slight post-yield softening followed by quick hardening is evident from the load-displacement curves, particularly those of PMMA at higher velocities. Whereas this trend is very distinct for PMMA, for PS there is a rather flat plateau of softening behavior before the hardening trend starts and ultimately for both materials at very high strains the network locks causing the code to terminate.

Figure A.3 (a, b) and Figure A.4 (a, b) shows the contours of plastic strain illustrating the penetration of the striker into the polymer and the consequent accumulation of plasticity in the same. Plastic deformation starts from near the impact location and spreads inwards; not much plasticity is witnessed near the constrained edge (e.g. where the polymer-film is attached to the substrate in erosion-resistant coatings). Plasticity is highest at the edges of the striker and the band of plasticity spreads inwards in a arc indicating that in the full specimen, the band from the two edges of the striker will meet (in the full specimen) and tend to separate out a region of relatively low plasticity near the impact location; it remains to be seen whether with the incorporation of a failure criteria this sort of behavior along with the associated element-deletion has the tendency to remove a chunk of the polymeric material thereby imitating a true erosion phenomena- the simulation of which remains the broader objective anyway. It is also

worth mentioning here that the contours of plastic strain for PS show some spurious spots of concentrated plasticity quite apart from the impact location (Figure A.4 (a, b)); the fact that such a behavior is consistent in most of the loading scenarios would indicate that this is because of some peculiar feature of PS over PMMA and not an oddity of the code itself, though this remain to be validated by further reasoning and/or investigation. A look at the contours of maximum principal stress (Figure A.3,4 (a, b)) suggests that near the impact point, local stresses are mainly compressive whereas beyond the striker on the traction free edge there are tensile stresses whose magnitudes increase with increasing impact velocity. Figure A.6 shows the plots of maximum values of tensile and compressive principal stresses (which play a significant role in polymer failure) with different impact velocities. The stresses in PMMA are higher than PS for all loading cases. Principal stress plays an important role in craze-failure and crack-formation; it remains to be seen whether this leads to micro-crack formation on the surface of the polymer films resulting in their erosion.



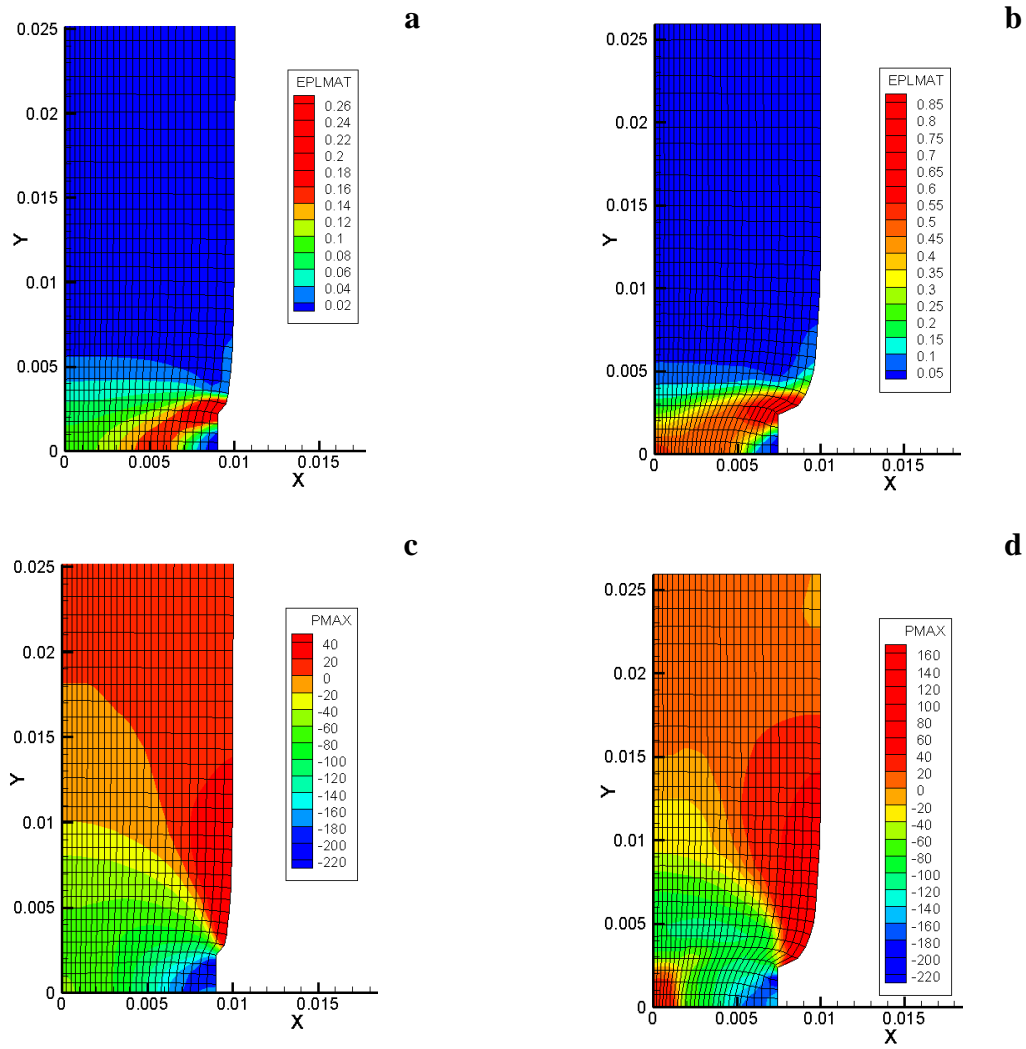


Figure A.3. Typical contours for PMMA.

Plastic Strain: (a) 10 m/s and (b) 50 m/s  
Maximum Principal Stress: (c) 10 m/s and (d) 50 m/s

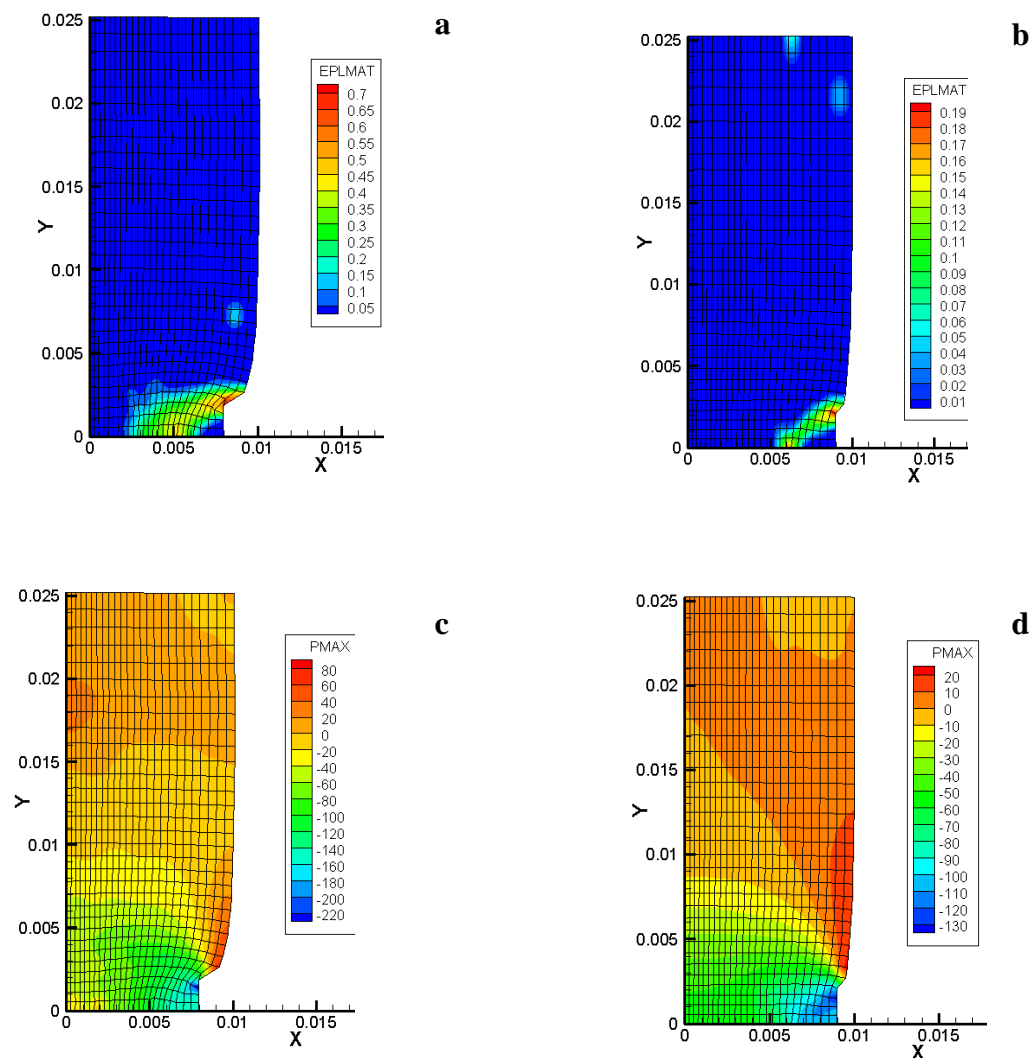


Figure A.4. Typical contours for PS.

Plastic Strain: (a) 10 m/s and (b) 50 m/s  
 Maximum Principal Stress: (c) 10 m/s and (d) 50 m/s

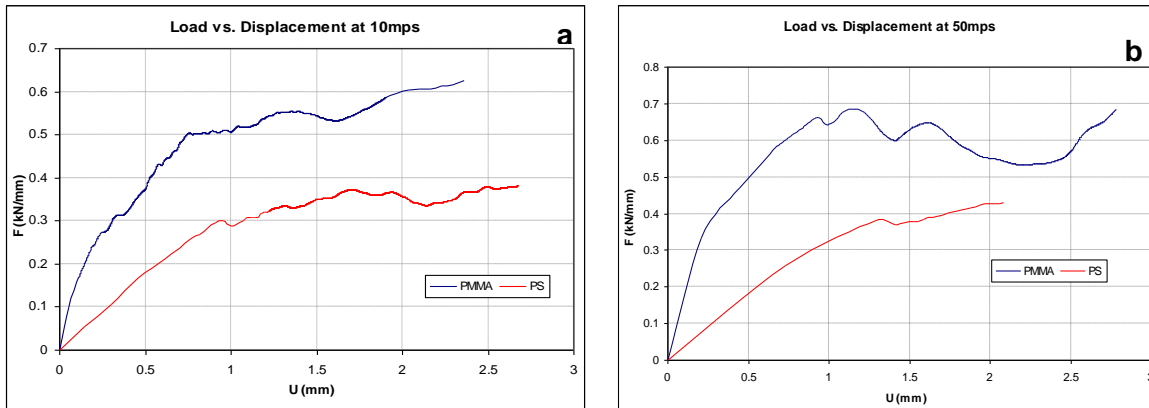


Figure A.5. Load vs. Displacement curves for materials PMMA and PS at different impact velocities (a) 10 m/s and (b) 50 m/s

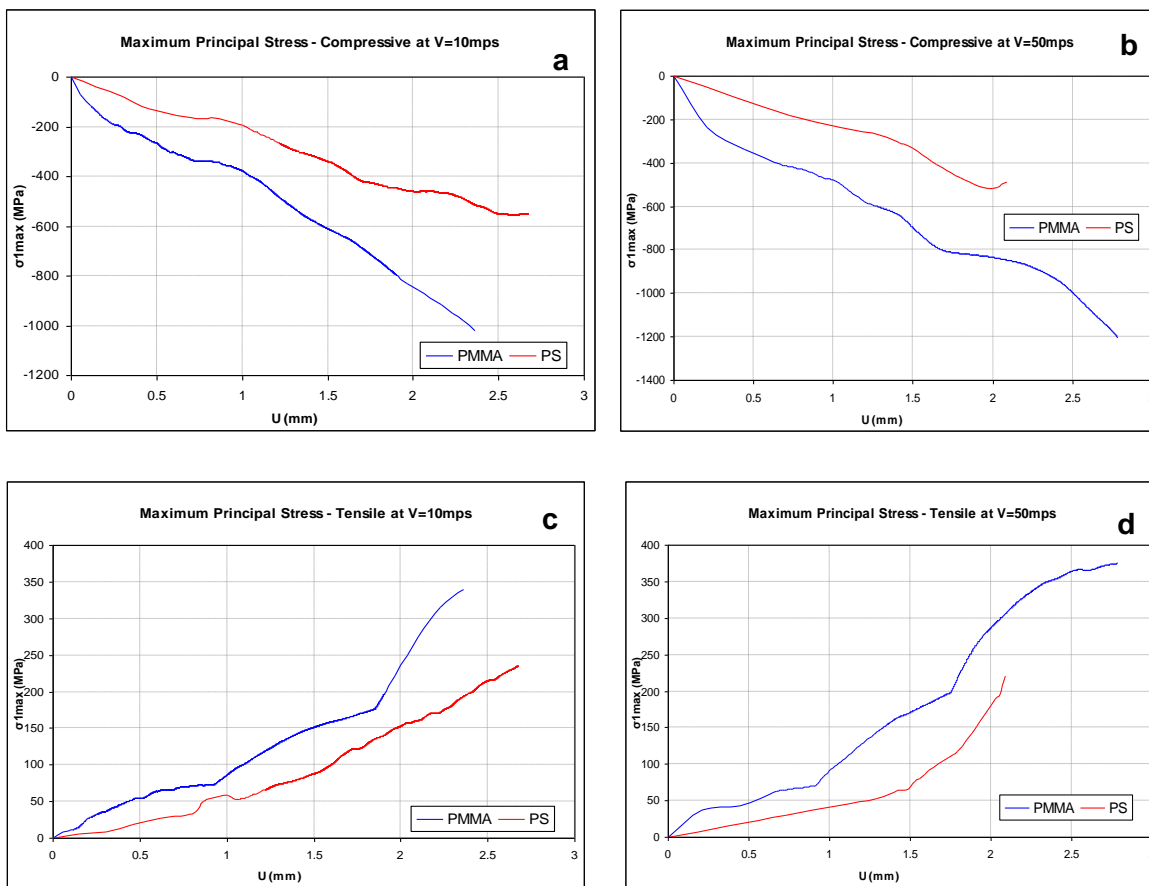


Figure A.6. Maximum Stress for PMMA and PS : Compressive (a) 10 m/s, (b) 50 m/s and Tensile (c) 10 m/s, (d) 50 m/s and (e) 50m/s.

An in-house non-linear FEA code using an advanced macromolecular model for polymers was used to study the monotonic impact response of polymeric coatings made of PMMA and PS. This endeavor can be extended to simulate the erosion process of polymeric structures by performing a parametric study on films of varied thicknesses subjected to a truly random loading with particles of arbitrary shape impacting at various velocities, angles of attack and at different locations etc. Thus this activity has paved a path to study the relative durability of polymeric coatings subject to erosion.

## **VITA**

Sourav Banerjee obtained a B.E. degree (gold medal) in Aeronautical Engineering from Anna University, India in the spring of 2007. He worked at the National Aerospace Laboratory, Bangalore for a year before joining an M.S. degree program in Aerospace Engineering at the Texas A&M University, College Station in the fall of 2008 under the guidance of Dr. Amine Benzerga and Dr. Ramesh Talreja. His primary interests are in the areas of mechanics of materials, constitutive modeling and impact simulation. Mr. Banerjee can be reached at: Department of Aerospace Engineering, H.R. Bright Building, Rm. 701, Ross Street - TAMU 3141, College Station, TX 77843. His email is: [sourav\\_banerjee@hotmail.com](mailto:sourav_banerjee@hotmail.com)